Using Self-Organizing Maps to Characterize Intraseasonal Transitions of the Wintertime Pacific Jet Stream

Maria M. Madsen[a], Jonathan E. Martin[a]

[a] Department of Atmospheric and Oceanic Sciences, *University of Wisconsin-Madison, Madison, WI, USA*

Corresponding author: Maria M. Madsen, mmmadsen@wisc.edu

ABSTRACT

Previous research regarding the intraseasonal variability of the wintertime Pacific jet has employed empirical orthogonal function (EOF)/principal component (PC) analysis to characterize two leading modes of variability: a zonal extension or retraction and a ~20° meridional shift of the jet exit region. These leading modes are intimately tied to the large-scale structure, sensible weather phenomena, and forecast skill in and around the vast north Pacific basin. Currently, however, transitions between these leading modes are poorly understood. Here, a self-organizing maps (SOM) analysis is applied to 71 Northern Hemisphere cold seasons of 250 hPa zonal winds from the NCEP/NCAR reanalysis data to identify 12 characteristic physical jet states and to explore the nature of intraseasonal transitions among such states of the north Pacific jet. Transition probability tables are calculated at 5-, 10-, 15-, and 20-day lags to identify common and uncommon transitions among the 12 SOM jet states. These analyses reveal that distinct, intraseasonal preferred transitions of the Pacific jet are identifiable at a variety of timescales. Composites of a number of preferred transitions at 10-day intervals suggest that the hitherto more common EOF/PC analysis of jet variability obscures important subtleties of jet structure, revealed by the SOM analysis, which bear on the underlying physical processes that the force transitions as well as the nature of their downstream impacts.

SIGNIFICANCE STATEMENT

Throughout Northern Hemisphere winter, the meandering Pacific jet stream routinely varies in its zonal and meridional extents directly impacting weather in Hawaii and North America while also influencing predictability. Previous studies have characterized this variability using a somewhat restrictive statistical method. We use a newer statistical technique that identifies the leading 12 archetypal jet structures observed in nature. We then use these 12 types to identify common and uncommon intraseasonal transitions among the structures. Our results show that there are preferred pathways by which the jet transitions within timescales ranging from 5-20 days. We describe the newly identified jet structures, the nature of the transitions among them, as well as their impacts on North American weather and medium-range forecast skill.

1. Introduction

Among the most ubiquitous and influential features of the general circulation of the atmosphere is the meandering, tropopause-level wind speed maxima known as the jet stream. The Northern Hemisphere (NH) jet stream is characterized by two regions of maximum intensity- one over the North Pacific extending from the coast of Asia into the central Pacific and another from the coast of North America into the Atlantic Ocean. During the NH winter [November-March (NDJFM)] when the meridional temperature gradient strengthens, both the climatological intensity and zonal extent of the north Pacific jet increase reaching their zeniths in February before weakening and retracting thereafter (Newman and Sardeshmukh 1998). Throughout the same season, the north Pacific jet undergoes large and often rapid variations in both its zonal extent as well as the meridional deflection of its exit region. These modes of variability of the Pacific jet have been the focus of a number of recent studies (e.g. Athanasiadis et al 2010; Jaffe et al. 2011; Griffin and Martin 2017; Breeden and Martin 2018; Winters el al. 2019a,b). As one of the most important features at the interface between the large-scale general circulation and the life cycle of individual weather systems, there is both theoretical and operational incentive to more comprehensively understand the details of jet variability.

Current understanding of the intraseasonal variability of the wintertime Pacific jet is centered on the two predominant modes mentioned above: a zonal extension or retraction of the jet exit region between 160°E to 120°W and a ~20° meridional shift of its exit region (Athanasiadis et al 2010; Jaffe et al 2011; Delcambre et al. 2013a) (Fig.1). These leading modes are associated with basin-scale anomalies in the Pacific that have substantial impact on the synoptic-scale structure and downstream sensible weather. For example, Chu et al. (1993) showed that a zonally retracted jet was associated with a wet Hawaiian winter, whereas an extended jet was associated with an extremely dry winter. Additionally, in constructing a climatology of subtropical Kona cyclones over Hawaii, Otkin and Martin (2004) found that a retracted Pacific jet is linked to increased frequency of such storms. Similarly, Jaffe et al. (2011) examined 19 cold season jet retractions that occurred within 28 years of NCEP/NCAR reanalysis data and found that variability within the Pacific storm track occurs in tandem with retraction events. Composite analysis of the retraction events revealed that prior to the retraction, enhanced storm track density downstream and poleward of the climatological jet exit region prevails. After the retraction events, however, the same region has suppressed storm track density, while enhanced storm track density appears in the central subtropical Pacific. Retraction events were also associated with a rapid onset of a negative Pacific-North America (PNA) pattern (Wallace and Gutzler 1981). Over the 10 days surrounding each event, both 500 hPa geopotential height and sea level pressure (SLP) anomalies switched polarity from negative to positive in the north Pacific, exhibited an equivalent barotropic structure with broad areal extent, and had magnitudes in excess of 200m and 20 hPa, respectively. Additionally, the composite 200-250 hPa Ertel potential vorticity (PV) anomaly field was rapidly deformed during the jet retraction events, suggesting that the evolution of tropopause-level PV anomalies may play an important role in initiating retraction events.

Breeden and Martin (2018) investigated the initiation of a long-lived Pacific jet retraction from mid-February to early March 2006 that preceded a persistent negative PNA pattern and led to record rainfall, flooding, and mudslides in Hawaii (Jayawardena et al. 2012). Using a quasi-geostrophic piecewise tendency analysis, they found that the retraction event was largely influenced by the deformation of a high-amplitude ridge downstream of an extended jet exit region. Key to the initiation of the retraction event were two anticyclonic anomalies in an area of strong deformation that, through a series of LC1 (Throncroft et al. 1993) wavebreaking events, diverted and retracted the jet. A negative PV anomaly on the cyclonic shear side largely influenced the growth of the ridge downstream of the jet exit region and the subsequent series of LC1 wavebreaking events.

In addition to sensible weather impacts in Hawaii and elsewhere in the Pacific basin, recent studies have demonstrated that intramodal changes of the Pacific jet have impacts over North America. Griffin and Martin (2017) showed that jet extensions and poleward shifts were both associated with enhanced 250 hPa cyclonic circulations in the central north Pacific and 850-hPa low-level warm anomalies over North America. For jet extensions, the warm anomalies were localized over western North America whereas for poleward shifts, they were localized over north-central North America. Conversely, jet retractions and equatorward shifts led to enhanced 250 hPa anticyclonic circulations in the central north Pacific and low-level cold anomalies over western North America. These results were corroborated by Winters et al. (2019a) who tied extreme temperature events (ETEs) in North America to the four Pacific jet regimes using a North Pacific jet (NPJ) phase diagram constructed from the two leading empirical orthogonal functions (EOFs) of 250 hPa zonal wind. They found that warm ETEs on the U.S. west coast are frequently characterized by an evolving jet extension and equatorward deflection in the 10 days preceding the event. Conversely, cold ETEs on the west coast and warm ETEs on the east coast occur most frequently in the days following jet retractions. This is consistent with studies showing negative PNA patterns associated with jet retraction events (e.g. Jaffe et al. 2011; Breeden and Martin 2018). Additionally, equatorward shifts of the jet preceded most cold ETEs on the U.S. east coast.

Using the same NPJ phase diagram employed in Winters et al. (2019a), Winters et al. (2019b) showed that the mode, and changes between modes, of the North Pacific jet have an apparent impact on medium-range forecast skill over North America. The study analyzed 30 years of Global

Ensemble Forecast System (GEFS) reforecasts to conclude that the greatest forecast skill occurred in conjunction with an extended or poleward deflected jet whereas the worst skill occurred in conjunction with a retracted or equatorward shifted jet. Additionally, there was reduced forecast skill when forecast periods occurred during a transition between extensions, retractions, and deflections poleward and equatorward.

Despite recent work demonstrating the substantial impact that Pacific jet variability has on the large-scale structure, sensible weather phenomena, and forecast skill in and around the vast North Pacific basin, the *transitions between the leading modes* of such variability are poorly understood. Better understanding of such transitions promises new insight into aspects of tropical/extratropical interaction and may provide additional guidance in the medium-range forecasting of some extreme events. As a step toward remedying this deficit of understanding, the present paper seeks to identify and characterize the most common wintertime Pacific jet transitions through application of self-organizing maps (SOM) (Kohonen 1982) and empirical orthogonal function/principal component (EOF/PC) analyses. The analysis consists of three components. First, the most common jet structures in the 71 winter seasons of the NCEP/NCAR Reanalysis data (Kalnay et al. 1996) are identified with a 12-node SOM analysis. Second, the SOM map is used to calculate transition probabilities amongst the 12 nodes on various timescales ranging from the sub-weekly to the sub-seasonal. Third, composites of the basin-wide extratropical structure and evolution of some selected, frequently occurring transitions will be constructed lending insight into the physical mechanisms driving specific transitions and the sensible weather associated with them.

The remainder of the paper is structured in the following way. Section 2 provides details of the dataset and methodology, including an in-depth description of the SOM analysis and transition probabilities. The structure of the various jet regimes revealed in the SOM analysis and their projections onto an EOF1/EOF2 phase space are analyzed in Section 3. Section 4 analyzes transition probabilities at 5-, 10-, 15-, and 20-day timescales. Composite analysis of the large-scale structure, evolution and downstream impacts of some specific 10-day transitions are detailed in Section 5. Lastly, Section 6 provides a discussion, summary, and future work.

2. Data and Methodology

The use of EOF analysis to decompose and filter spatiotemporal data is a common form of exploratory data analysis that has long been a central part of weather and climate research. EOF/PC analysis identifies a hierarchy of orthogonal spatial patterns most representative of the modes of variability within a state space (the EOFs), as well as a time-series of coefficient values for each EOF that represents the magnitude of the EOF's contribution to the state space through time (the principal components, or PCs) (e.g., Lorenz 1956; Kutzbach 1967; Cohen 1983; Smith et al. 1996; Hannachi 2004; Wilks 2011). The leading EOFs are the patterns explaining the largest amount of variance of the dataset. Wintertime Pacific jet variability has been traditionally studied employing EOF/PC analysis (e.g. Athanasiadis et al. 2010; Jaffe et al. 2011; Griffin and Martin 2017; Winters et al. 2019a, 2019b). Previous work has identified the leading mode, EOF 1, as an extension/retraction, with anomalies nearly along the climatological jet exit region (Fig. 1a). The next leading mode, EOF 2, is characterized by anomalies displaced poleward or equatorward of the exit region (Fig. 1b) (Delcambre et al. 2013a).

Although previous research on jet variability has relied heavily upon EOF analysis, the leading patterns explain only ~30% of the total variance and, by construction, each mode is linearly independent from the other. Therefore, EOF analysis provides a rather static view of Pacific jet *transitions*. Transitions within the Pacific jet involve nonlinear processes (e.g. Breeden and Martin

2019) that are not captured through EOF/PC analysis alone. Identifying commonly observed transitions requires an analysis technique that objectively identifies the physically observed patterns and captures the nonlinearities of the data. Consequently, this study also employs a self-organizing maps (SOM) analysis. SOM analysis is free from the orthogonality constraint of EOF/PC analysis and captures nonlinear (nonorthogonal) distributions of the zonal wind. The inclusion of both linear and nonlinear aspects is a significant advantage of the SOM. This statistical technique has been applied to meteorological data sets in both synoptic-climatologies (e.g. Hewitson and Crane 2002; Hope et al. 2006; Lynch et al. 2006; Cassano et al. 2006; Reusch et al. 2007; Schuenemann et al. 2009; Johnson and Feldstein 2010) as well as examinations of climate model output (e.g. Skific et al. 2009a,b ; Schuenemann and Cassano 2009, 2010; Gervais et al. 2016). The use of SOMs in this study provides a less subjective, more physical and versatile visualization tool for characterizing transitions that compliments, rather than replaces, the traditional EOF/PC analysis.

a. Self-Organizing Maps

SOMs is a method within the field of artificial neural networks that organizes large, multi-dimensional datasets into finite arrays of recurring *physical* patterns (Kohonen, 2001). Unlike EOF/PC analysis and other cluster methods in which the data is assumed to be stationary, SOM treats the data as a continuum. The SOM in this study uses daily 250 hPa zonal winds from the NCEP/NCAR Reanalysis (Kalnay et al. 1996) available at a 2.5°x 2.5° horizontal resolution. It covers 71 cold seasons (1948/49-2018/19) in which a cold season is defined as November 1 through March 31 (NDJFM). The spatial domain is 100°E to 120°W and 10° to 80°N which covers nearly all of the North Pacific basin.

The SOM is trained through an unsupervised iterative process that begins with a grid of generalized patterns distributed across a user-determined number of nodes (archetypal states) (Kohonen, 2001). The generalized patterns are defined by reference vectors that are linearly initialized using the leading eigenvectors of the 250 hPa zonal wind, where nodes within close spatial proximity are referred to as neighboring nodes. A training period ensues in which the input vectors of daily zonal wind are read into the SOM and matched to the reference vector of greatest similarity (smallest Euclidean distance between the input and reference vector). The reference vector of greatest similarity, also referred to as the best matching unit (BMU), updates to include properties of the newly assigned input vector. A self-learning process continues to update both the nodes with properties of the assigned input vectors as well as reference vectors of neighboring nodes to maximize differences between neighboring nodes. The amount of adjustment within a node is determined by a time-decreasing learning rate, and the adjustment of neighboring nodes is determined through a neighborhood function with a time-decreasing radius.

The SOM in this study utilizes batch training, as it is the most computationally efficient with larger datasets (Kohonen 1998; Vesanto et al. 2000; Liu et al. 2006). Unlike sequential training, the batch training process does not specify a learning rate function; rather, the weight vector, m_i, adjusts the reference vectors by:

$$m_i(t+1) = \frac{\sum_{j=1}^{M} n_j h_{ij}(t)\overline{x_j}}{\sum_{j=1}^{M} n_j h_{ij}(t)} \quad (1)$$

where M is the user-determined number of groups into which the data is partitioned, t is each learning iteration, $\overline{x_j}$ is the mean of the n input vectors within the current group, and h_{ij} is the neighborhood function. An Epanechikov neighborhood (‘ep’) function is selected for its higher performance in comparison to three other neighborhood functions available in the Matlab SOM toolbox (Vesanto et al. 2000; Liu et al. 2006). The 'ep' function updates neighboring nodes by,

$$h_{ci} = \max(0{,}1 - (\sigma_t - d_{ci})^2), \qquad (2)$$

in which a neighborhood radius of influence at time t, σ_t, is specified, and d_{ci} is the distance between SOM nodes c and i. The SOM is run with two sets of trainings of decreasing neighborhood radius. The initial batch training uses a larger neighborhood radius of influence equal to the size of the smaller SOM grid dimension. The training iterates for 10 times the length of the input vector and creates a broad pattern distribution. A second training specifies a smaller neighborhood radius of 1 and fine-tunes the SOM nodes based on the distribution from the resultant initial batch training. The SOM iterates through this process until a mean quantization error is minimized for the entire collection of nodes. The end result is a large SOM array comprised of the updated reference vectors which is then converted into a 2D matrix of maps. The resulting matrix of nodes consists of the most representative physical patterns spanning the continuum of, in this analysis, the zonal 250 hPa winds.

The tunable parameters in the SOM, including grid size, number of iterations, neighborhood radius, and initialization, are selected to achieve a balance of low average quantization error (QE) and topographic error (TE) as well as an evenly distributed Sammon map (Sammon 1969). The QE quantifies the difference between the node average and the input vectors wherein lower QE values indicate a better representation of the BMU to the data. Every SOM node consists of a collection of input vectors with varying QEs as well as a mean QE. Another key map quality measure is TE, which measures the percentage of input vectors that do not have a neighboring second BMU. In a SOM map, the nodes closest to one another are most similar, and therefore, the smaller the TE, the better the SOM map quality. Lastly, a Sammon map illustrates the Euclidian distances between each node in the SOM grid on a 2D distortion plane (Sammon, 1969). A quality SOM map will have a balance of low QE and TE, and a flat, evenly distributed Sammon map.

The present work employs a 3x4 SOM grid consisting of 12 nodes. Smaller grid sizes (2x3, 3x3) led to a blending of relevant patterns whereas larger grid sizes (4x4, 4x5) yielded patterns not easily distinguishable from one another. Therefore, a 3x4 grid size includes enough interpretable patterns to examine transitions while maintaining low QE and TE errors (Table 1) and a well distributed Sammon map (Fig. 2).

b. Transition Probabilities

Transition probabilities between SOM nodes are computed to identify common and uncommon transitions at varying time scales. The analysis considers 5-, 10-, 15-, and 20-day transition probabilities in order to elucidate differences between rapid transitions and longer two-to-three-week transitions. Transition probabilities are computed using a first order Markov chain,

$$P_{ij}(n) = P\{\boldsymbol{X}_{t+n} = j \mid \boldsymbol{X}_t = i\}, \quad (3)$$

in which the probability of transitioning into node j at lag n only depends on the initial node i. Thus, for the daily winds within node j at $t = 0$, the total number of transitions to nodes 1-12 by the end of that interval[1] is tabulated. These values are referred to as transition totals, and there are 12 per starting node for each time interval. Next, the 12 transition totals are divided by the number of days in the complete time series that are occupied by the starting node to give a probability of

[1] The transition total includes only days in which the 5, 10, 15, and 20-day intervals are within the same NDJFM season.

each SOM node transitioning into any of the 12 nodes within the time lag of interest. For example, node 4 (a zonally extended jet, see Fig. 4), is identified in 797 of the 10,721 NDJFM days in the 71-year NCEP time series. These days represent starting points for 797 forward trajectories. The 10-day transition analysis totals the number of trajectories that end up in nodes 1-12 in the subsequent 10-day interval. The total for each node is divided by 797 to determine the 10-day probabilities of transition into node 1, node 2, and so on. A similar procedure yields transition probabilities for any N-day interval.

Following the work of Gu and Gervais (2020), statistical significance of the transition probabilities is determined through a Monte Carlo sampling method. The null hypothesis is that transitions between the 12 SOM nodes are random. In order to reject the null hypothesis, unconditional probabilities are produced by sampling 100 random days from the dataset and calculating the frequency of occurrence (FOC) of each SOM node within the sample. This is repeated 100,000 times to yield a distribution of FOC for every SOM node. A student's two-tailed t test is then performed to identify the transition probabilities above the 95% significance level.

3. North Pacific Jet Regimes

a. Leading EOF/PC modes of variability

The leading modes of wintertime Pacific jet variability obtained from the present analysis are consistent with previous findings, with EOF 1 (describing 19% of the variance) characterized by anomalies nearly along the climatological jet exit region (Fig. 3a), while EOF 2 (describing 11% of the variance) is characterized by anomalies displaced poleward or equatorward of the exit region (Fig. 3b). It is worth noting that the anomalies depicted in the positive phase of EOF1 (hereafter referred to as EOF 1+) show both an extension of the jet as well as a slight equatorward deflection. The negative phase of EOF 1 (EOF 1-), however, illustrates a combination of a jet retraction and poleward deflection into the Aleutian Islands. Conversely, the phases of EOF 2 illustrate a poleward deflection of the jet exit region south of the Aleutian Islands (EOF 2+) or an equatorward deflection stretching west of Hawaii (EOF 2-).

b. North Pacific jet SOM nodes

In conducting a SOM analysis of the 250 hPa zonal wind, 12 intraseasonal jet anomaly regimes are depicted in the SOM nodes with a FOC representing the portion of days falling within the associated node (Fig. 4). Nodes closest to one another depict more similarity whereas nodes furthest apart depict the largest differences (e.g. nodes 1 and 12). The EOF-based leading modes of variability are evident within the SOM grid. Nodes 8 and 5 correspond to the positive and negative phase of EOF 1, respectively, with anomalies centered nearly along the jet exit region. Nodes 10 and 2 resemble the positive and negative phase of EOF 2. The nodes resembling EOF 2 show slightly larger FOC than the nodes corresponding to EOF 1. Apart from the nodes resembling the leading EOF patterns, node 6 depicts a split jet with a positive anomaly centered over the Gulf of Alaska and the highest FOC of all 12 nodes. The second highest FOC is illustrated by node 7, with positive anomalies centered in the eastern half of the climatological jet indicating an enhancement of the jet exit region. Strong jet extensions are depicted in nodes 4, 8 and 12. However, node 4 illustrates an extension with an equatorward deflection, while the positive anomalies in nodes 8 and 12 are more poleward of node 4 by 5° and 10°, respectively. Nodes 9, 10, and 11 depict varying poleward deflections. Nodes 9 and 10 occur more frequently, with positive anomalies stretching north of 35° (node 10) or 40° (node 9) and negative anomalies stretching along the equatorward edge of the climatological jet. Equatorward deflections are evident in nodes 2 and 3, with a more NW to SE tilt of the anomalies in node 3. Lastly, node 1 depicts the strongest negative anomalies in the jet exit region and weaker positive anomalies centered at 50°N and 15°N.

To further illustrate the relationship between the two leading EOF/PC patterns of the North Pacific jet and the SOM patterns, days with a QE at or below the mean QE of the entire SOM grid are projected onto an EOF/PC 2D phase space in Fig. 5. Following the NPJ phase space developed in Winters et al. (2019b), the leading two PCs serve as the axes of the phase space wherein the *x*-axis is defined by PC1 (jet extension with minor equatorward displacement/jet retraction with poleward enhancement), and the y-axis is defined by PC2 (poleward/equatorward deflection). For many of the SOM nodes, there is a clear clustering in a specific quadrant of the phase space. Nodes 4, 8, and 12 cluster on the right half of the phase space, with node 8 clustering nearly along the positive x-axis (jet extension), node 4 clustering slightly below the positive x-axis (equatorward deflected jet extension), and node 12 clustering above the positive x-axis (poleward deflected jet extension). Conversely, nodes 1, 5, and 9 cluster on the left half of the phase space, with node 5 clustering along the negative x-axis (retraction), node 1 clustering below the negative x-axis (retraction and equatorward deflection) and node 9 clustering above the negative x-axis (retraction and poleward deflection). The clustering of nodes 10 and 11 show the strongest similarities to the poleward deflected EOF 2+ pattern, whereas nodes 2 and 3 cluster nearly along the equatorward deflected EOF 2- axis. Nodes 6 and 7 depict the weakest anomalies and are represented as a weak jet retraction and a weak jet extension in the phase space, respectively. However, the SOM pattern depicts node 6 as a split jet near the exit region and node 7 as an enhanced jet stream -synoptic details which are poorly represented in the phase space. Therefore, despite consistencies between the leading EOF/PC modes of Pacific jet variability and many of the SOM nodes in this analysis, the subtleties of Pacific jet variability are far better represented by the SOM than by the traditional EOF/PC phase space.

4. Transition Probabilities

In order to elucidate more and less frequent transitions, transition probabilities are analyzed at shorter 5-day timescales (Fig. 6a), medium 10-day timescales (Fig. 6b), and extended 15-day and 20-day timescales (Fig. 6c and 6d). Statistically significant enhanced (reduced) transition probabilities are depicted in red (blue) boxes to illustrate preferred (unlikely) pathways for each of the 12 SOM nodes.

a. 5-Day Transitions

The 5-day transition probability table (Fig. 6a) illustrates that a majority of the SOM nodes are more likely to persist than transition into another node in this short interval. The increased likelihoods of persistence range from 21% (nodes 12 and 3) to 46% (node 9). There are only 2 nodes that have an equal or increased probability of transitioning into another node. Node 3, which depicts an equatorward deflection with slight extension, has a 21% likelihood of remaining in node 3 and a higher 22% likelihood of transitioning into the neighboring node 2. The stronger extension with a slight equatorward deflection denoted by node 4, however, has equal 30% probabilities of persisting or transitioning into neighboring node 8, an extension 5° poleward of the node 4 extension. Nodes depicting extended regimes (4,8,12) also have increased likelihood of transitioning into other extended states. Node 12, for example, has a 19% likelihood of deflecting poleward to a more poleward extended state (node 11) and a 14% likelihood of deflecting equatorward into the strong extension illustrated by node 8. These same extended states (4, 8, 12) all show decreased likelihood of transitioning into retracted states (nodes 1, 5, 9). Likewise, the retracted states exhibit little likelihood of transitioning into extended states (nodes 4, 8, 12). Instead, they are most likely to persist or transition into a neighboring node of a similar retracted anomaly pattern.

Every node within the 5-day probability table has at least two significant preferred transition pathways except for nodes 6 and 7. Node 6, depicting the positive anomaly in the Gulf of Alaska, exhibits only an increased likelihood of persisting (31%). However, it has decreased likelihoods of transitioning into strong extensions (4, 8) and strong retractions (5, 9). Similarly, node 7 shows only an anomalous likelihood of persisting (28%), along with a number of low probability transitions into regimes with negative anomalies at or south of the climatological jet exit region (nodes 1, 5, 9, 10). Overall, at timescales at and below 5-days, it is most likely that the Pacific jet will either persist or undergo a minimal transition into a neighboring node.

b. 10-Day Transitions

By 10-days, the number of statistically significant transition probabilities decreases slightly (Fig. 6b). With the exception of node 7, persistence at this interval is still a substantial tendency with significant probabilities ranging from 13% for node 12 to 31% for node 9. However, at this longer interval, many of the nodes are more likely to transition into nearby nodes than persist. For example, node 12 has ~15% likelihood of transitioning into nearby nodes 8 or 11, a 20% likelihood of transitioning into node 7, and only a 13% likelihood of persisting. Similarly, node 4 is most likely to transition into node 8 at 30% compared to the 14% probability of either persisting or transitioning into node 12. The significant high probabilities for node 5 are more evenly distributed between persisting or transitioning to nodes 9 or 10.

Similar to 5-day transitions, nodes depicting extended states (4, 8, 12) are unlikely to transition into, or from, retracted states (5, 9). Rather, they tend to transition 5-10° poleward or equatorward into a similar anomaly pattern. An exception to this general tendency is node 12, which has the largest probability of transitioning from its extended and poleward deflected state to a pattern with positive anomalies confined to the eastern half of the climatological jet (node 7).

c. 15-Day Transitions

At extended-range timescales, the number of statistically significant transitions decreases even further (Fig. 6c). Persistence is still evident with percentages near 20% in nodes depicting poleward deflections (nodes 9, 10) and a strong extension (node 8). Other than persisting or transitioning to a nearby node, the poleward deflections in nodes 9 and 10 have no other preferred pathways. The strong extension in node 8, however, also has preferred pathways towards an equatorward deflection (node 2) or a weakening of the extension (node 7). Node 5 loses the tendency to persist by 15-days and has only one significant probability (20%) of transitioning 10-15° equatorward to node 10. It is also worth noting that the poleward and retracted nodes 5, 9, and 10 are states for which half of the SOM nodes have significant reduced probabilities (nodes 2, 3, 4, 7, 8, 11, and 12). This was evident in shorter 5-day to medium 10-day transition periods as well, suggesting that it is uncommon for equatorward deflections of the jet stream (2, 3, 4) or strong extensions (4, 8, 12) to transition into poleward deflections west of the dateline. Additionally, a reversal of anomalies from nodes 5 and 9 to nodes 4 and 8 remains unlikely.

d. 20-Day Transitions

At longer 20-day timescales, most nodes still have 3 or more significant transition probabilities. Only one third of the SOM nodes exhibit notable persistence, with the strong extension in node 8 topping the list with persistence likelihood at 19%. The preferred pathways for neighboring nodes 4 and 8 differ largely at this timescale. Node 4, which has the largest number of statistically significant transition probabilities, has the largest transition likelihood to node 7 at

23% and two other preferred pathways- persistence or transitioning to node 12. Node 8, conversely, has preferred pathways to an equatorward state (node 2), a similar node 4 state, or persistence. These tendencies suggests that the jet is more likely to transition equatorward than it is poleward in a given 20-day interval. Consistent with this preference, the reduced likelihoods of transitioning to retracted and poleward deflected states 5, 9, and 10 are still evident at 20-days for over half of the SOM nodes (2, 3, 4, 7, 8, 11, and 12).

e. Preferred Transitions

The transition probabilities depicted in Fig. 6 demonstrate that transitions within the wintertime Pacific jet are not random; rather, there are transitions that are more likely and less likely to occur at short, medium, and extended timescales. At short to medium 5- and 10-day transition times, almost every node has a tendency to persist. The increased likelihood for persistence is especially strong throughout the 20-day transition period for the extension depicted in node 8 and the poleward deflection depicted in node 9. Also notable is that for timescales of 10-days and under, all preferred transitions occur into adjacent nodes, and very few nodes have preferred transitions into the weaker anomaly states of nodes 6 and 7. Importantly, this suggests that relaxation towards a near-climatological state in such intervals is not a preferred tendency.

For nodes in the lower left SOM grid (5, 9, 10), there is a consistent preferred tendency to transition from node 5 to 9 and 10, and node 9 to 10 at short, medium, and longer timescales. This counterclockwise motion through the SOM grid suggests that a retracted and poleward deflected jet will likely shift equatorward into a more canonical poleward deflected jet regime that more closely resembles EOF 2-. Node 9 is the only poleward deflected state with an increased likelihood of transitioning even more poleward into node 5; however, it does not remain a preferred transition at extended 15- and 20- day timescales. In fact, it is unlikely for most of the nodes to transition into the poleward states of 5, 9, and 10. The preferred transitions for the species of retracted jet denoted by node 1, however, are very different from those of the node 5 retraction. Instead of transitioning into nodes 9 or 10, node 1 is most likely to transition into the equatorward deflected state denoted by node 2 or a near-climatological split jet denoted by node 6 at medium range timescales. Equatorward states illustrated by nodes 2 and 3, on the other hand, are preferred transition states not only from adjacent nodes at medium and extended timescales, but also from weaker anomaly states (nodes 6 and 7) and a strong extended state (node 8).

In focusing on unlikely transitions, the shorter 5-day to medium range 15-day probability tables illustrate that nodes depicting robust jet extensions (nodes 4, 8) are unlikely to transition into, or from, a retracted jet (nodes 1, 5, 9). Therefore, the more commonly studied transitions between an extended jet and retracted jet (e.g. Jaffe et al. 2019; Breeden and Martin 2018; Breeden and Martin 2019) are rare when compared to other transitions. Rather, it appears that strong extensions and retractions are more likely to deflect meridionally.

5. Composites

To illustrate the evolution of the synoptic scale environments associated with the aforementioned preferred Pacific jet transitions, a composite analysis for 10-day transitions is performed from nodes resembling the leading EOFs- namely, node 8 (EOF 1+), node 5 (EOF 1-), and node 2 (EOF 2-). The selection of 10-day transitions from these three SOM nodes provides a basis for comparison to prior research on characteristic environments of jet variability on medium-range timescales determined from EOF analysis. The composites include only those days that are contained within a single season and that have a QE within 1σ of the mean SOM QE at the start of the transition. Composite maps are then constructed at days -10, -5, 0, 5, and 10 in which day 0 is the start of the 10-day transition within a specific node, and day 10 is the end of the 10-day transition into another node. Anomalous quantities of 500 hPa geopotential heights, SLP, 850 hPa temperature, and 250 hPa zonal winds are analyzed to characterize regional circulation changes and downstream impacts of different preferred pathways. A two-tailed Student's t test is applied to determine statistically significant features at the 95% confidence level.

a. Jet Extension (Node 8) 10-Day Transitions

Node 8, depicting a strong jet extension, is likely to persist or transition equatorward into node 4 at 10-days, with its persistence likelihood exceeding that of transitioning into node 4. Throughout the 20-day period of node 8 persistence, there are strong surface (Figs. 7f-j) and 500 hPa (Fig. 7a-e) cyclonic anomalies supporting a strong jet extension on the equatorward flank of the upper-level height anomaly. Additionally, there is an upper-level cyclonic anomaly downstream over the eastern half of the US with an associated subtropical jet enhancement over the southeastern U.S. (Fig. 7 a-e). A weak anticyclonic anomaly appears at 500 hPa over British Colombia on day -5 and persists over the remaining 15 days (Fig. 7 c-e). The development of this upper-level positive height anomaly suggests a transition into a positive PNA-like pattern (Wallace and Gutzler 1981). Additionally, the jet extension is evident as early as day -10, suggesting the extension triggers the PNA pattern. There are widespread negative temperature anomalies at 850 hPa extending from Mongolia and China to the central Pacific (Fig. 7 f-j). The negative anomalies are strongest between lags -10 and 0 and weaken above a weakening positive SLP anomaly (Fig. 7 g-h). There is also a small localized 2K anomaly straddling the border of Yukon and British Colombia on day 0 and 10 as well as a -2K anomaly over eastern North America (Fig. 7h-j).

In comparison, the 10-day transition from node 8 to 4 is characterized by a positive PNA-like pattern only on day 0, with an equivalent barotropic structure characterizing the strong upper-level cyclonic anomaly extending across the north Pacific, the anticyclonic anomaly over northwestern North America, as well as another cyclonic anomaly over the eastern half of North America (Fig. 8c, h). Unlike the composites for node 8 persistence, the strong anticyclonic anomaly over British Colombia first appears on day 0, and from day 0 to 10, the cyclonic anomaly shifts equatorward as the anticyclonic anomaly retrogresses (Fig 8c-e). By day 10, the 500 hPa anomalies adopt a meridional dipole structure over the North Pacific wherein the positive zonal wind anomalies are shifted 5° equatorward (Fig 8e). The retrogression of the anticyclonic anomaly is central to shifting the jet extension equatorward and occurs as the cyclonic anomaly over the eastern U.S becomes stronger and more isotropic (Fig. 8 d-e). Below the isotropic anomaly are 850 hPa negative temperature anomalies of -4K over northeastern North America that extend further northwest from lag 0 to lag 10 (Fig. 8h-j). Additionally, the positive 2K anomaly over northwestern North America dissipates by lag 10. Overall, the differences between the node 8 persistence and transition to node 4 suggests that the slight equatorward shift in the transition to node 4 is associated with a decay of a positive PNA event and stronger low-level negative temperature anomalies over North America.

b. Jet Retraction (node 5) 10-Day Transitions

The jet retraction in node 5, characterized by negative anomalies nearly along the climatological jet exit and positive anomalies poleward of 45°N, has almost equal probability of persisting, transitioning 5° equatorward into node 9, or transitioning 10° equatorward into node 10 at 10-day transition times. During the node 5 persistence, two 500 hPa height maxima over the North Pacific on day -10 merge into a zonally elongated anticyclonic anomaly by day 0 that stretches over the western north Pacific and supports negative zonal wind anomalies on its southern flank (Fig. 9 a-c). Downstream, another upper-level anticyclonic anomaly is located over the eastern US (Fig. 9 a-e). Temperature perturbations at 850 hPa depict warm anomalies between 2 and 6 K over eastern Asia, the western Pacific basin, and eastern North America that are strongest between days -10 and 0 (Fig 9 f-j). Both the upper- and lower-level patterns of the node 5 10-day persistence resemble that of the extended node 8 persistence but with opposite sign.

The transition from node 5 to 9 begins on day 0 (Fig. 10 c,h) with a synoptic scale pattern similar to that of day 10 in the node 5 persistence (Fig 9 e,j). The upper-level anomaly has a slight SW to NE tilt over the Pacific, and the SLP anomaly is centered near 180°W (Fig 10 c,h). However, the upper- and lower-level anticyclonic anomalies weaken between days 0 and 5, and by day 10, the upper-level anomaly has shifted 5° equatorward into a more zonally oriented anticyclonic anomaly (Fig. 10 c-e). Both the negative and positive zonal wind anomalies shift equatorward as well. Also notable is the stronger 500 hPa anticyclonic anomaly over eastern North America throughout the transition in comparison to a 10-day node 5 persistence. The stronger upper-level anomaly is associated with stronger low-level warm anomalies over North America between days 5 and 10, whereas the warm anomalies over eastern Asia and the western Pacific are similar to the node 5 persistence (Fig 10 f-j). At the surface there is a cyclonic anomaly over eastern Asia on day -10 that propagates NE over Russia and into North America over the 20-day period, while the anticyclonic anomaly in the central Pacific weakens between days 0 and 10 (Fig. 10 f-j).

The final preferred transition from node 5 to node 10 is associated with a more rapid decay of the upper- and lower-level anticyclonic anomalies between days 0 and 10 (Fig. 11 c,d,e & h,i,j). The weakening of the upper-level geopotential height anomaly by day 5 is accompanied by a weakening and equatorward shift of both the positive and negative zonal wind anomalies. By the end of the 10-day transition, the anticyclonic anomaly is confined to the climatological jet exit region, and the zonal wind anomalies shift an additional 5° equatorward (Fig. 11 e). Low-level warm anomalies also weaken between days 0 and 10. Comparison of the node 5 preferred pathways of almost equal likelihood demonstrate that the transitions equatorward to 9 and 10 are associated with weakening upper- and lower-level anticyclonic anomalies throughout the transition.

c. Equatorward Deflection (node 2) 10-Day Transitions

The equatorward deflection that characterizes node 2 resembles EOF 2-. At 10 days, node 2 is most likely to persist, transition to node 1 as a stronger retraction with both poleward and equatorward positive zonal wind anomalies, or deflect poleward to a NW-SE tilt east of the climatological jet exit region denoted by node 3. In the 10-day persistence composite, there is an anticyclonic anomaly south of the Aleutians that grows from day -10 to day 0 (Fig. 12 a-c, f-h) and then weakens gradually from day 0 to 10 (Fig. 12 c-e, h-j). The growing anticyclonic anomaly supports the strengthening of both a positive zonal wind anomaly on its poleward flank and a negative zonal wind anomaly on its equatorward flank. At the surface, a strong positive SLP anomaly centered south of the Aleutians induces cold-air advection in northeasterly flow over Canada with widespread cold anomalies between -2 to -4 K from days -10 to 5 (Fig. 12 f-j). The equatorward shift of the jet is associated with a 500 hPa cyclonic anomaly that extends NE from 20°N at the dateline to the U.S. west coast (Fig. 12 a-e).

Unlike the persistence of node 2, the transition from node 2 to 1 is characterized by a strengthening upper-level anticyclonic anomaly south of the Aleutians from day -10 to day 0 (Fig. 13 a-c). Additionally, the anomaly and its associated SLP anomaly retrogress and zonally expand between day 0 and 10 (Fig. 13 c-e, h-j). The strengthening, retrogression, and zonal expansion of the anticyclonic anomaly support a strong retraction in the jet exit region and an enhancement of zonal winds between 45 and 60°N. Directly south of the anticyclonic anomaly is a small cyclonic anomaly as well as a larger cyclonic anomaly further downstream over the west coast of the U.S.

as early as day -10 (Fig. 13 a-e). The separate cyclonic anomalies at day -10 merge by day 0 and become coincident with an enhancement of the equatorward shifted jet. In the lower-levels, 850 hPa warm air anomalies grow to 6K over eastern Asia, and a weak warm air anomaly develops through central North America by day 10 (Fig. 13 f-j). Cold air anomalies persist off the U.S west coast between day -10 and 10 (Fig. 13 f-j).

Lastly, the transition to node 3 is characterized by a sudden onset of a 500 hPa anticyclonic anomaly on day 0 that shifts northeastward over the 10-day transition (Fig. 14 c-e). The upper-level cyclonic anomaly extends further west than in the other node 2 transitions at days 0 and 5 and breaks off into two separate anomalies by day 10 (Fig. 14 a-e). At the surface, the positive SLP anomaly shifts NE as well and is associated with a warm air anomaly on its western flank and stronger cold air anomalies over Canada from days 0 to 10 (Fig. 14 f-j). Comparison of node 2 preferred transitions show that although they are all tied to anticyclonic anomalies, the extratropical evolutions and downstream impacts vary substantially between transition composites.

6. Discussion

In this study, a novel self-organizing maps analysis is applied to 250 hPa zonal winds over 71 NDJFM cold seasons to better understand intraseasonal transitions of the wintertime Pacific jet. Prior work in understanding intraseasonal Pacific jet variability has proceeded from identification of the leading modes of variability: a zonal extension or retraction and a meridional deflection of the jet exit region, as depicted in EOF/PC analysis (e.g. Athanasiadis et al. 2010; Jaffe et al. 2011; Griffin and Martin 2017; Breeden and Martin 2018; Winters et al. 2019a, 2019b). The SOM analysis described here expands and compliments previous EOF/PC analysis, as it provides a more detailed and versatile tool to examine jet variability. The SOM identifies 12 archetypical Pacific jet patterns resembling variations of the extended/retracted and poleward/equatorward deflected patterns of Pacific jet variability described in prior EOF-based analyses (e.g., Schubert and Park 1991; Athanasiadis et al. 2010; Jaffe et al. 2011), as well as new complex modes of variability not captured by these previous analyses. These include an enhancement of the jet characterized by node 7, a tilted, equatorward deflected jet characterized by node 3, and a split jet with a downstream wind speed maximum in the Gulf of Alaska denoted by node 6.

These 12 SOM nodes serve as initial state jet patterns in which the temporal evolution is traced through the SOM space to characterize common and uncommon transitions. Transition probabilities are quantified through probability tables which indicate the conditional probability that the jet will reside within any SOM node after a specific time interval given the initial SOM node. The probability tables from shorter 5-day intervals to longer 20-day intervals demonstrate that there are preferred transitions that vary between 5-, 10-, 15-, and 20-day lags. At shorter 5-day transition times, most of the SOM nodes are more likely to persist than to transition into other nodes. By 10 days, persistence is still likely for many of the nodes, though most also exhibit substantial likelihoods of transitioning into nearby nodes, consistent with the transient behavior of the jet stream. By extended-range timescales of 15 days to 20 days, the persistence signature drops dramatically while most preferred transitions are still confined to adjacent nodes.

Directional transitions through the SOM space, indicated by high transition probabilities consistently in specific SOM nodes throughout the 5- to 20-day interval, can indicate predictable underlying dynamics driving preferred transitions. In particular, the retracted and poleward deflected nodes 5, 9, and 10, have a consistent tendency to transition in a counterclockwise direction through the SOM space (i.e., high transition probabilities from nodes 5 to 9 and 10, 9 to

10, and 10 to 11). This directional transition implies that a retracted jet with a positive poleward anomaly is most likely to transition equatorward into a more canonical poleward deflected jet resembling EOF 2+. In contrast to this tendency from a retracted poleward deflected jet, the node 1 retraction with both poleward and equatorward positive anomalies is most likely to transition into node 2, a weaker retraction with an equatorward deflection, or node 6, a more climatological structure. Of all of the nodes, these two seemingly separate retraction types (nodes 1 and 5), have the most consistent preferred transitions from medium to extended time scales. Preferred transitions for other nodes differ more substantially between timescales.

Composite analysis comparing preferred transitions of extended, retracted and equatorward deflected jet regimes at the 10-day interval demonstrate that there are distinct differences in the synoptic scale circulation and impacts between each transition. Even with subtle transitions of the jet, there are widespread and sometimes strong 850 hPa temperature and SLP anomalies that develop over 5 to 20 days. Consistent with prior research on jet retractions (e.g. Jaffe et al. 2011; Griffin et al. 2017, Breeden and Martin 2018), the composite structure of various preferred transitions from node 5 show a dominant elongated anticyclone in the central Pacific. However, the downstream temperature anomalies differ from the analyses in Griffin et al. (2017) and Winters et al. (2019a) in that there are no cold anomalies over the western/northwestern part of North America. Additionally, the node 5 composites feature warmer anomalies over eastern/northeastern US than prior analyses of EOF/PC-identified retractions (Griffin et al. 2017; Winters et al. 2019a). Differences from prior analyses in low-level temperature anomalies are evident in transition composites of nodes 8 and 2 as well. For example, the low-level temperature anomalies associated with node 8 (Fig. 7c, 8c) are consistent with previous studies (Griffin et al. 2017; Winters et al. 2019a). However, in the transition to node 4, the warm anomalies over Alaska and the Pacific

Northwest dissipate as an upper-level anticyclonic anomaly retrogresses from a positive PNA-like structure. The composite differences in synoptic-scale features and downstream impacts highlight the importance of more carefully distinguishing between jet regimes, as these features likely have their origin in characteristic tropical and extratropical interactions. Ongoing case study investigation of these transitions will likely provide additional insight into the physical processes and interactions driving preferred transitions.

Subtleties of the SOM nodes and transitions between them may also help to advance understanding of the impact of Pacific jet variability on medium range forecasts skill through an application of the SOM-based analysis presented in this study to the examination recently undertaken by Winters et al. (2019b). In comparing the best to the worst GEFS medium-range forecasts initialized during the four EOF/PC-identified North Pacific jet regimes, Winters et al. (2019b) revealed that there were key differences in the synoptic-scale structure within each regime. For example, for forecasts initialized during an extended regime, the worst forecasts emerged from a synoptic-scale environment resembling that of SOM node 8 and a positive PNA-like structure (Winters et al. 2019b, their Fig. 12b), whereas the best forecasts emerged from an environment more characteristic of SOM node 4 (Winters et al. 2019b, their Fig. 12a). This suggests that subtle 5-10° latitudinal displacements of the Pacific jet extension are likely tied not only to specific teleconnections like the PNA but also to downstream, medium-range forecast skill.

Additionally, although forecasts initialized during retractions had the highest forecast errors in comparison to the other three jet regimes, the subset of retractions that led to the best forecasts were characterized by zonal wind and geopotential height anomalies characteristic of SOM node 5 (Winters et al. 2019b, their Fig. 12c), which subsequently evolved towards a poleward extension (Winters et al. 2019b, their Fig. 14c). This is consistent with the node 5 preferred transitions into poleward deflected states of 9 and 10. The subset of retractions that lead to the worst forecasts, however, were characterized by more negative geopotential heights and a positive zonal wind anomaly in the subtropics (Winters et al. 2019b, their Fig. 12d)- an environment more characteristic of SOM node 1. The reduced forecast skill could be associated with the divergent preferred transitions of node 1 into a more equatorward deflected state of node 2 or into a more climatological structure denoted by node 6.

The differences in forecast skill between extended and retracted regimes highlighted in Winters et al. (2019b) taken with the differences in preferred transitions between regimes illustrated in the SOM probability tables suggest that previous analysis of jet variability blends important jet structures with varying underlying processes and teleconnections. Further separation of jet variability into the 12 SOM nodes provides a more detailed representation of the wintertime Pacific jet that can be utilized to investigate transitions and their relationship to teleconnection patterns like the PNA, Madden Julian Oscillation (MJO), and El Niño-Southern Oscillation (ENSO) that have been tied to the structure of the Pacific jet (e.g. Madden and Julian 1971, 1972; Wallace and Gutzler 1981; Barnston and Livezey 1987; Franzke and Feldstein 2005; Athanasiadis et al. 2010; Wettstein and Wallace 2010; Franzke et al. 2011). Assessment of such teleconnections, in addition to discerning the roles of tropical versus extratropical processes in driving preferred transitions of the Pacific jet can add considerable value to both medium-range forecasts and sub-seasonal to seasonal forecasts. Future work will employ a linear inverse model to determine the optimal precursors for all 12 wintertime jet states described by the SOM nodes. Comparison of these optimal precursors to composites of preferred transitions will lend insight into the physical processes governing specific transitions as well as their predictability.

Acknowledgments.

Support for this work is provided by the National Science Foundation under grant NSF-16400455 as well as from Ned P. Smith Professorship of Climatology (granted to the second author) by the University of Wisconsin-Madison. The authors would like to thank Professors Daniel Vimont, Stephanie Henderson, and Michael Morgan at the University of Wisconsin-Madison and Professor Melissa Gervais at Pennsylvania State University for their insightful discussions and constructive feedback. Additionally, anonymous reviews have provided valuable suggestions and comments for the presentation of this work.

Data Availability Statement.

NCEP Reanalysis data is provided by the NOAA/OAR/ESRL PSL, Boulder, CO and available at https://psl.noaa.gov/data/gridded/data.ncep.reanalysis.html.

REFERENCES

Athanasiadis, P. J., J. M. Wallace, and J. J. Wettstein, 2010: Patterns of wintertime jet stream variability and their relation to the storm tracks. *Journal of the Atmospheric Sciences*, **67**, 1361–1381, https://doi.org/10.1175/2009JAS3270.1.

Barnston, A. G., and R. E. Livezey, 1987: Classification, seasonality, and persistence of low-frequency atmospheric circulation patterns. *Monthly Weather Review*, **115**, 1083–1126, https://doi.org/10.1175/1520-0493(1987)115<1083:CSAPOL>2.0.CO;2.

Breeden, M. and J. E. Martin, 2018: Analysis of the initiation of an extreme North Pacific jet retraction using piecewise tendency diagnosis. *Quarterly Journal of the Royal Meteorological Society*, **144(715)**, 1895–1913, https://doi.org/10.1002/qj.3388.

Breeden, M., and J. E. Martin, 2019: Evidence for nonlinear processes in fostering a North Pacific jet retraction. *Quarterly Journal of the Royal Meteorological Society*, **145**, 1559–1570, https://doi.org/10.1002/qj.3512.

Cassano, E. N., A. H. Lynch, J. J. Cassano, and M. R. Koslow, 2006: Classification of synoptic patterns in the western Arctic associated with extreme events at Barrow, Alaska, USA. *Climate Research*, **30**, 83–97, https://doi.org/10.3354/cr030083.

Chu, P. A. J. Nash, and F. Porter, 1993: Diagnostic studies of two contrasting rainfall episodes in Hawaii: Dry 1981 and wet 1982. *Journal of Climate*, **6**, 1457–1462, https://doi.org/10.1175/1520-0442(1993)006<1457:DSOTCR>2.0.CO;2.

Cohen, S. J., 1983: Classification of 500 mb height anomalies using obliquely rotated principal components. *Journal of Applied Meteorology*, **22(12)**, 1975-1988, https://doi.org/10.1175/1520-0450(1983)022<1975:COMHAU>2.0.CO;2.

Delcambre, S., D. Lorenz, , D. Vimont, , and J. Martin, 2013: Diagnosing Northern Hemisphere jet portrayal in 17 CMIP3 global climate models: Twentieth-century intermodel variability. *Journal of Climate*, **26**, 4910–4929, https://doi.org/10.1175/JCLI-D-12-00337.1.

Franzke, C., and S. B. Feldstein, 2005: The continuum and dynamics of Northern Hemisphere teleconnection patterns. *Journal of the Atmospheric Sciences*, **62**, 3250–3267, https://doi.org/10.1175/JAS3536.1.

Franzke, C., T. Woollings, and O. Martius, 2011: Persistent circulation regimes and preferred regime transitions in the North Atlantic. *Journal of the Atmospheric Sciences*, **68**, 2809 – 2825, https://doi.org/10.1175/JAS-D-11-046.1.

Gervais, M., E. Atallah, J. R. Gyakum, and L. Bruno Tremblay, 2016: Arctic air masses in a warming world. *Journal of Climate***, 29 (7)**, 2359–2373, https://doi.org/10.1175/JCLI-D-15-0499.1.

Griffin, K. S., and J. E. Martin, 2017: Synoptic features associated with temporally coherent modes of variability of the North Pacific jet stream. *Journal of Climate*, **30**, 39–54, https://doi.org/10.1175/JCLI-D-15-0833.1.

Gu, Q., and M. Gervais, 2020: Exploring North Atlantic and North Pacific Decadal climate prediction using self-organizing maps. *Journal of Climate*, **34(1)**, 123–141. https://doi.org/10.1175/JCLI-D-20-0017.1.

Hannachi, A., 2004: A primer for EOF analysis of climate data. University of Reading, 33 pp.

Hewitson, B. C., and R. G. Crane, 2002: Self-organizing maps: Applications to synoptic climatology. *Climate Research*, **22 (1)**, 13–26, https://doi.org/10.3354/cr022013.

Hope, P. K., W. Drosdowsky, and N. Nicholls, 2006: Shifts in synoptic systems influencing south west Western Australia. *Climate Dynamics*, **26**, 751–764, https://doi.org/10.1007/s00382-006-0115-y.

Jaffe, S. C., J. E. Martin, D. J. Vimont, and D. J. Lorenz, 2011: A synoptic climatology of episodic, subseasonal retractions of the Pacific jet. *Journal of Climate*, **24**, 2846–2860, https://doi.org/10.1175/2010JCLI3995.1.

Jayawardena, I.M., Y. L. Chen, A.J. Nash, and K. Kodama, 2012: A comparison of three prolonged periods of heavy rainfall over the Hawaiian islands. *Journal of Applied Meteorology*, **51**, 722–744, https://doi.org/10.1175/JAMC-D-11-0133.1.

Johnson, N. C. and S. B. Feldstein, 2010: The continuum of North Pacific sea level pressure patterns: Intraseasonal, interannual, and interdecadal variability. *Journal of Climate*, **23**, 851-867, https://doi.org/10.1175/2009JCLI3099.1.

Kalnay, E., and Coauthors, 1996: The NCEP/NCAR 40-Year Reanalysis Project. *Bull. Amer. Meteor. Soc.*, **77**, 437–471, https://doi.org/10.1175/1520-0477(1996)077<0437:TNYRP>2.0.CO;2.

Kohonen, T., 1982: Self-organized formation of topologically correct feature maps. *Biological Cybernetics*, **43 (1)**, 59–69, https://doi.org/10.1007/BF00337288.

Kohonen, T., 1998: The self-organizing map. *Neurocomputing: An International Journal, **21***(**1-3)**, 1–6, https://doi.org/10.1016/S0925-2312(98)00030-7.

Kohonen, T., M. R. Schroeder, and T. S. Huang, Eds., 2001: *Self-Organizing Maps*. 3rd ed., Springer-Verlag, Berlin, Heidelberg.

Kutzbach, J. E., 1967: Empirical eigenvectors of sea-level pressure, surface temperature and precipitation complexes over North America. *Journal of Applied Meteorology and Climatology*, **6(5)**, 791-802, https://doi.org/10.1175/1520-0450(1967)006<0791:EEOSLP>2.0.CO;2.

Liu, Y.,R. H. Weisberg, and C. N. Mooers, 2006: Performance evaluation of the self-organizing map for feature extraction. *Journal of Geophysical Research: Oceans*, **111 (C5)**, https://doi.org/10.1029/2005JC003117.

Lorenz, E. N., 1956: Empirical orthogonal functions and statistical weather prediction. Statistical Forecasting Project Report 1, Dept. of Meteor., MIT. 49pp.

Lynch A., O. Uotila, and J. J. Cassano, 2006: Changes in synoptic weather patterns in the polar regions in the 20th and 21st centuries, part 2: Antarctic, *International Journal of Climatology*, **26**(9), 1181–1199, https://doi.org/10.1002/joc.1305.

Madden, R. A., and P. R. Julian, 1971: Detection of a 40–50 day oscillation in the zonal wind in the tropical Pacific. *Journal of the Atmospheric Sciences*, **28**, 702–708, https://doi.org/10.1175/1520-0469(1971)028<0702:DOADOI>2.0.CO;2.

Madden, R. A., and P. R. Julian, 1972: Description of global-scale circulation cells in the tropics with a 40–50 day period. *Journal of the Atmospheric Sciences*, **29**, 1109–1123, https://doi.org/10.1175/1520-0469(1972)029<1109:DOGSCC>2.0.CO;2.

Newman, M., and P. D. Sardeshmukh, 1998: The impact of the annual cycle on the North Pacific/North American response to remote low-frequency forcing. *Journal of the Atmospheric Sciences*, **55**, 1336– 1353, https://doi.org/10.1175/1520-0469(1998)055<1336:TIOTAC>2.0.CO;2.

Otkin, J. A., and J. E. Martin, 2004: The large-scale modulation of subtropical cyclogenesis in the central and eastern Pacific Ocean. *Monthly Weather Review*, **132**, 1813–1828, https://doi.org/10.1175/1520-0493(2004)132<1813:TLMOSC>2.0.CO;2.

Reusch, D. B., R. B. Alley, and B. C. Hewitson, 2007: North Atlantic climate variability from a self-organizing map perspective. *Journal of Geophysical Research Atmospheres*, **112 (D2)**, https://doi.org/10.1029/2006JD007460.

Sammon, J. W., 1969: A nonlinear mapping for data structure analysis. *IEEE Transactions on Computers*, **18**, 401–409, https://doi.org/10.1109/T-C.1969.222678.

Schubert, S. D., and C.-K. Park, 1991: Low-frequency intraseasonal tropical–extratropical interactions. *Journal of the Atmospheric Sciences*, **48**, 629–650, https://doi.org/10.1175/1520-0469(1991)048<0629:LFITEI>2.0.CO;2.

Schuenemann, K., J. Cassano, and J. Finnis, 2009: Forcing of precipitation over Greenland: Synoptic climatology for 1961–99, *Journal of Hydrometeorology*, **10**, 60– 78, https://doi.org/10.1175/2008JHM1014.1.

Schuenemann, K. C., and J. J. Cassano, 2009: Changes in synoptic weather patterns and Greenland precipitation in the 20th and 21st centuries: 1. Evaluation of late 20th century simulations from IPCC models. *Journal of Geophysical Research,* **114**, D20113, https://doi.org/10.1029/2009JD011705.

Schuenemann, K. C., and J. J. Cassano, 2010: Changes in synoptic weather patterns and Greenland precipitation in the 20th and 21st centuries: 2. Analysis of 21st century atmospheric changes using self-organizing maps. *Journal of Geophysical Research,* **115**, D05108, https://doi.org/10.1029/2009JD011706.

Skific, N., J. A. Francis, and J. J. Cassano, 2009a: Attribution of projected changes in atmospheric moisture transport in the Arctic: A self-Organizing map perspective. *Journal of Climate*, **22(15)**, 4135–4153, https://doi.org/10.1175/2009JCLI2645.1.

Skific, N., J. A. Francis, and J. J. Cassano, 2009b: Attribution of seasonal and regional changes in Arctic moisture convergence. *Journal of Climate*, **22(19)**, 5115-5134, https://doi.org/10.1175/2009JCLI2829.1.

Smith, T. M., R. W. Reynolds, R. E. Livezey, and D. C. Stokes, 1996: Reconstruction of sea surface temperature using empirical orthogonal functions, *Journal of Climate,* **9**, 1403-1420, https://doi.org/10.1175/1520-0442(1996)009<1403:ROHSST>2.0.CO;2.

Thorncroft C, Hoskins BJ, McIntyre ME. 1993. Two paradigms of baroclinic wave life cycle behaviour. *Quarterly Journal of the Royal Meteorological Society,* **119**, 17–55, https://doi.org/10.1002/qj.49711950903.

Vesanto, J., J. Himberg, E. Alhoniemi, and J. Parhankangas, 2000: SOM toolbox for Matlab 5. Helsinki University of Technology Tech. Rep. A57, 60 pp.

Wallace, J. M., and D. S. Gutzler, 1981: Teleconnections in the geopotential height field during the Northern Hemisphere winter. *Monthly Weather Review,* **109**, 784–812, https://doi.org/10.1175/1520-0493(1981)109<0784:TITGHF>2.0.CO;2.

Wettstein, J. J., and J. M. Wallace, 2010: Observed patterns of month-to-month storm track variability and their relationship to the background flow. *Journal of the Atmospheric Sciences*, **67**, 1420–1437, https://doi.org/10.1175/2009JAS3194.1.

Wilks, D. S., 2011: *Statistical Methods in the Atmospheric Sciences*, Vol. 100. Academic press, 648 pp.

Winters, A. C., L. F. Bosart, and D. Keyser, 2019a: Antecedent North Pacific jet regimes conducive to the development of continental U.S. extreme temperature events during the cool season. *Weather Forecasting*, **34**, 393–414, https://doi.org/10.1175/WAF-D-18-0168.1.

Winters, A. C., D. Keyser, and L. F. Bosart, 2019b: The development of the North Pacific jet phase diagram as an objective tool to monitor the state and forecast skill of the upper-tropospheric flow pattern. *Weather Forecasting*, **34**, 199–219, https://doi.org/10.1175/WAF-D-18-0106.1.

TABLES

SOM Grid Size	*Quantization Error*	*Topographic Error*
2x2	437	3%
3x3	400	3.6%
3x4	395	3%
4x4	390	5%
5x4	385	3%

Table 1. Quantization and topological error of SOM grid for various grid sizes.

FIGURES

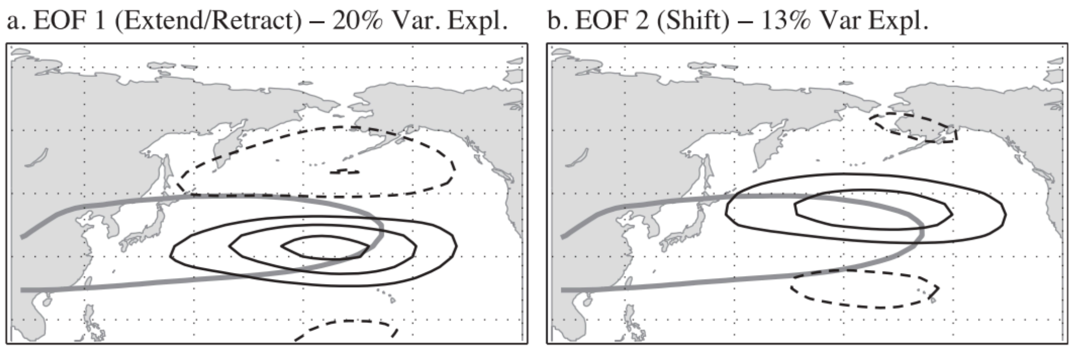

Figure 1. Leading two EOFs of 300 hPa zonal wind from 20°-80° N regressed onto the zonal wind field from 0°-80° N. Contours are every $4 ms^{-1}$ and zero line removed. Solid (dashed) lines are positive (negative) perturbations and the gray contour is the $20\ ms^{-1}$isotach of the 300 hPa mean NDJFM zonal wind. (Figure and caption adapted from Delcambre et al., 2013a).

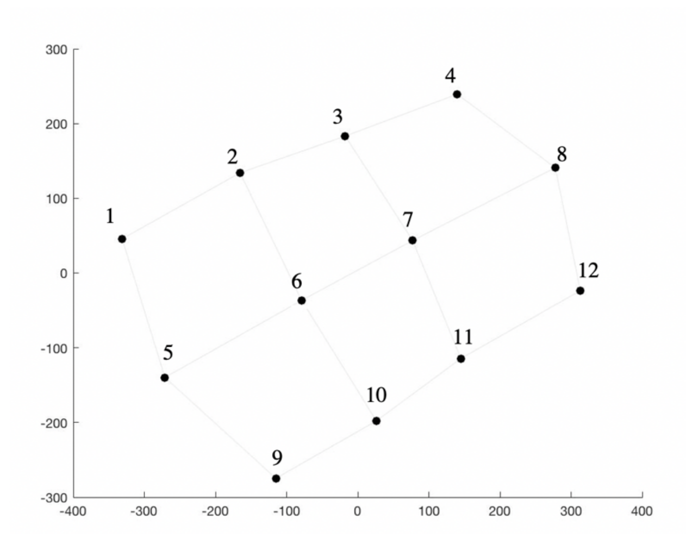

Figure 2. Sammon Map of Euclidean distances between nodes in the 3x4 SOM grid shown in Fig. 4.

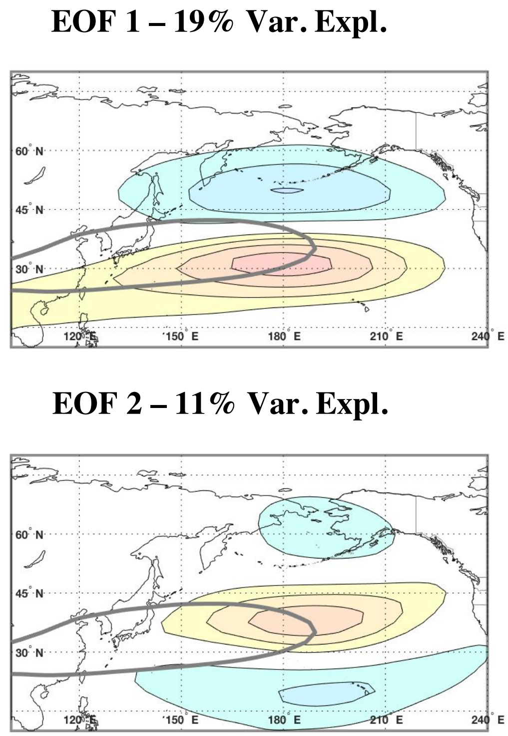

Figure 3. EOF pattern of the 250 hPa zonal wind over the North Pacific. Perturbations are shaded (ms^{-1}) every 4 starting at 4 (-4). Mean 40 ms^{-1} isotach over the 71 cold seasons is contoured in grey. (top) EOF1 (bottom) EOF2.

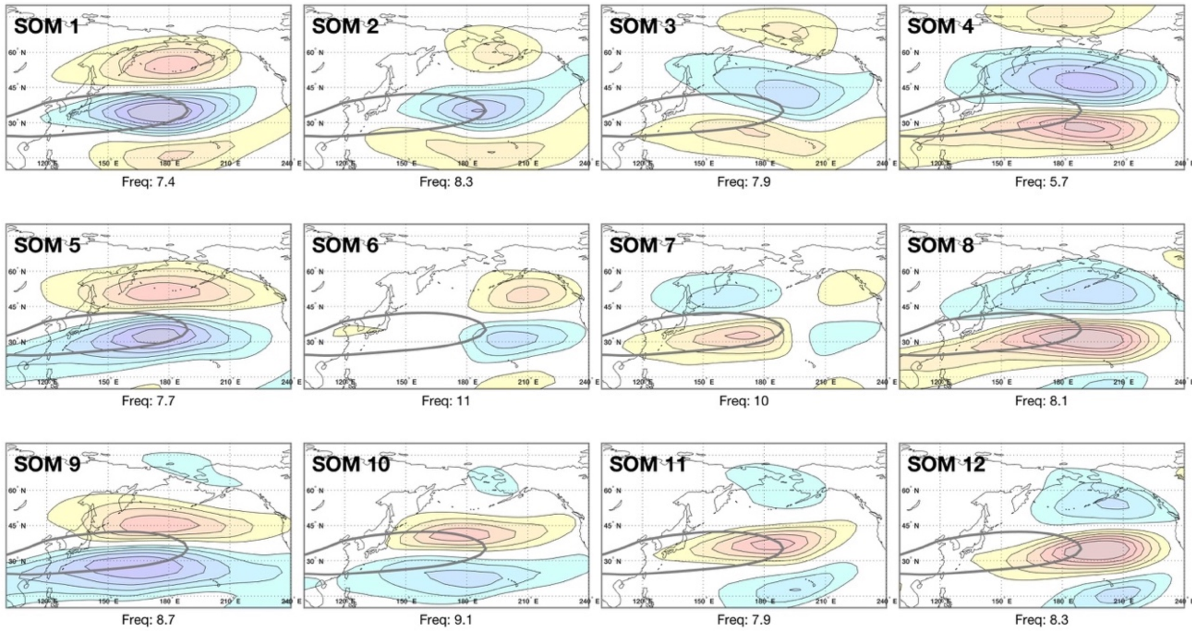

Figure 4. SOM grid of 12 most recurring patterns of the wintertime Pacific basin 250 hPa zonal wind. Anomalies of the 250 hPa isotachs (ms^{-1}) are shaded in warm (cool) colors every 4 starting at 4 (-4). The mean 71 cold season 40 ms^{-1} isotach is in gray. Below each node is the associated frequency of occurrence (in %) relative to all other nodes.

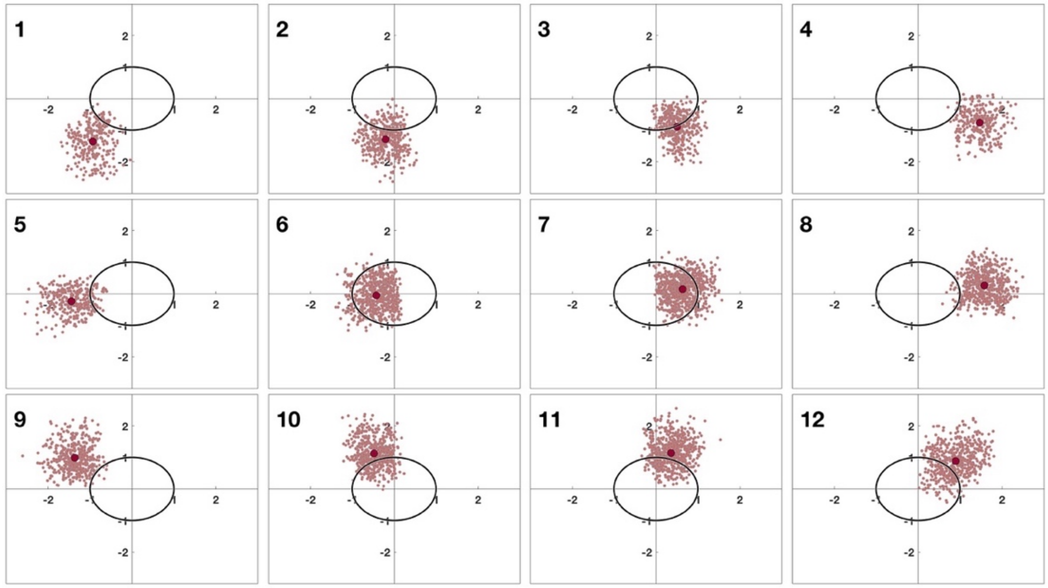

Figure 5. State of the daily Pacific jet (maroon circles) in the 2D phase space of the leading 250 hPa zonal wind PCs for every day comprising each of the 12 SOM nodes within the 71 cold seasons (1948/49-2018/19). Black circles represent the 2 and 4 contours of magnitude in the EOF/PC phase space.

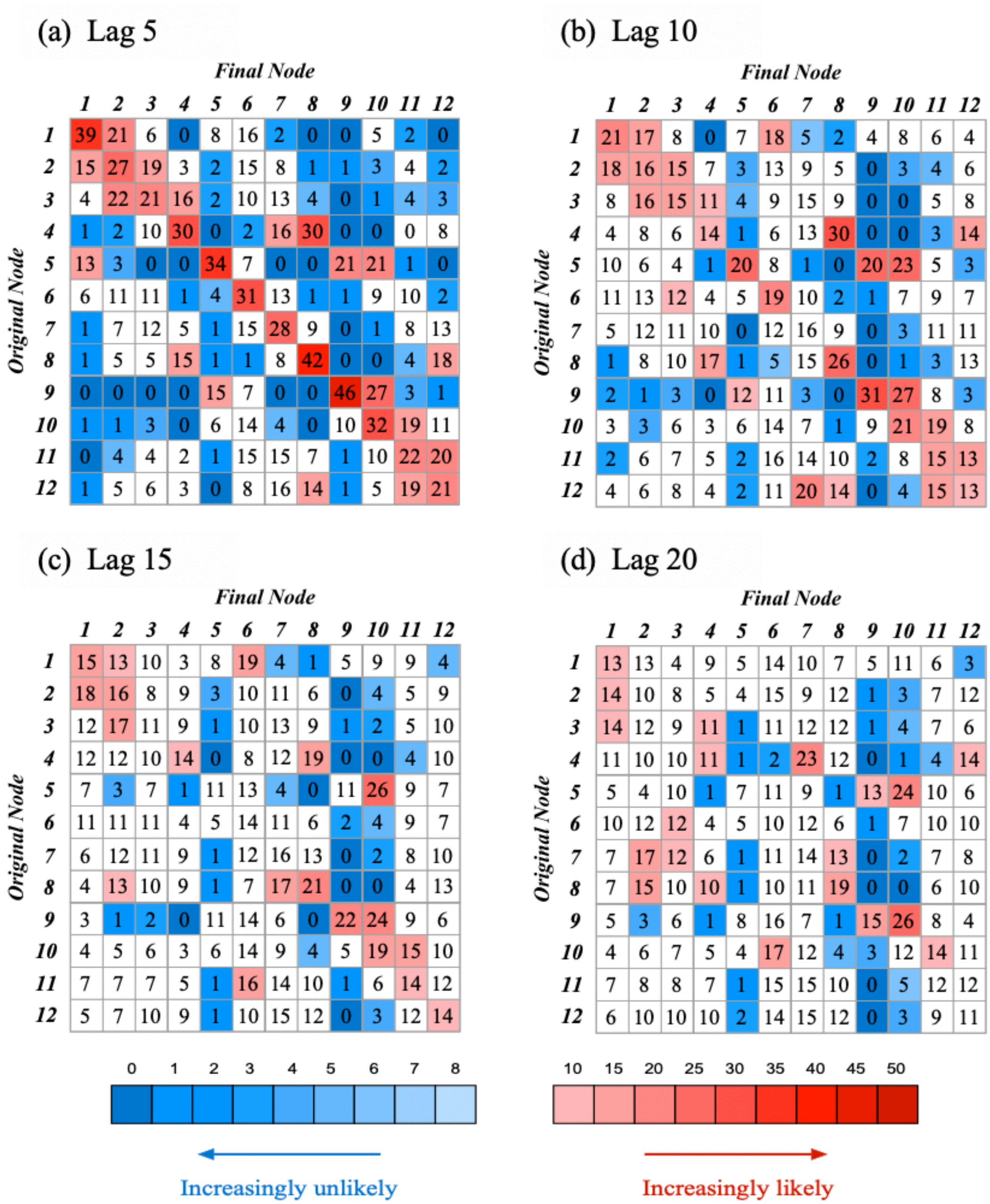

Figure 6. 5-20-day anomalous transition probabilities for SOM Nodes 1-12 observed in the NCEP Reanalysis data. Within each subplot, columns 1-12 correspond to the SOM Node into which the transition is observed and rows 1-12 correspond to the node at the start of the transition. Red (blue) squares indicate enhanced (reduced) transition frequency at the 95% significance level.

Node 8 10-Day Persistence

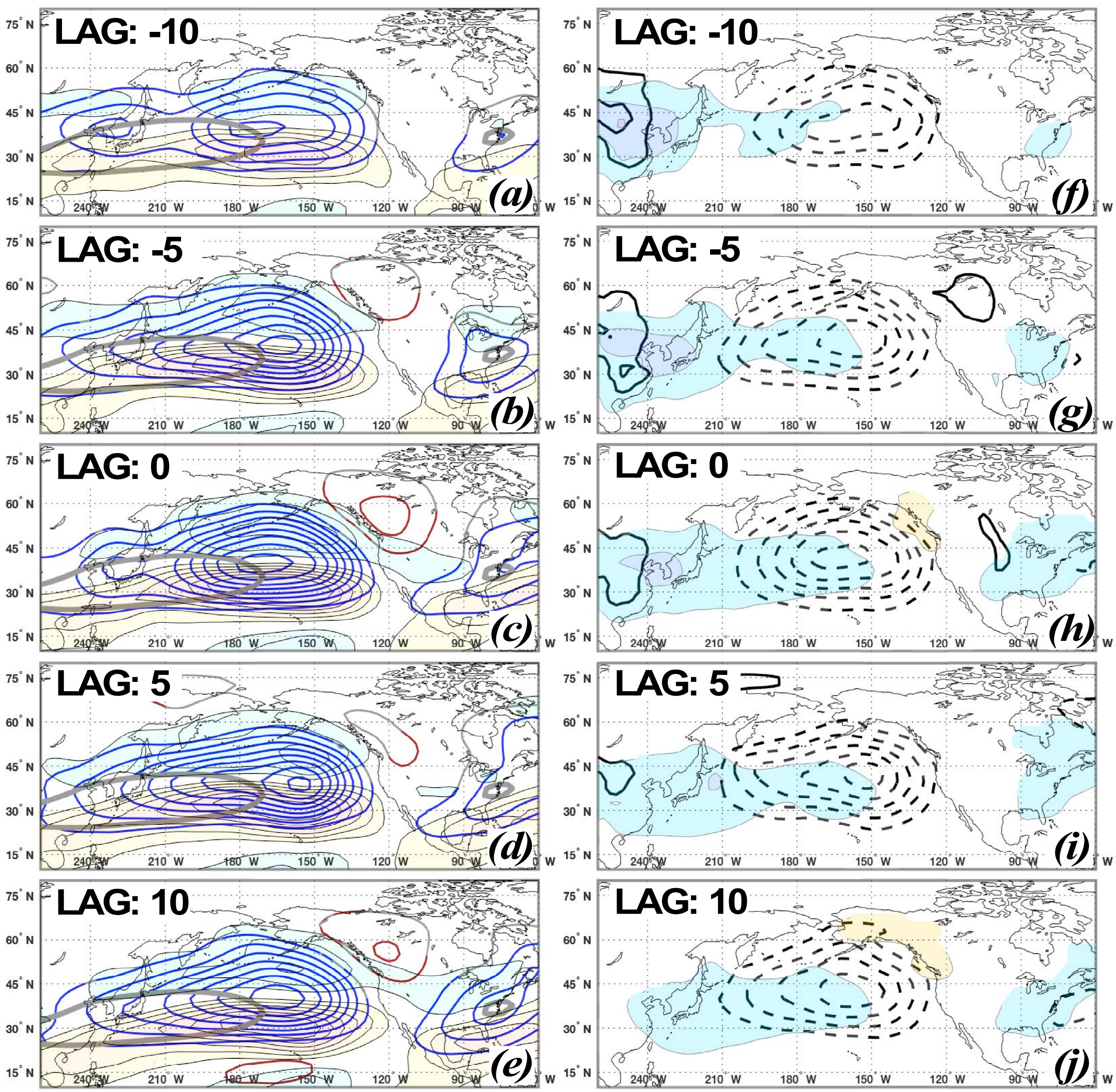

Figure 7. Composite large-scale features of SOM node 8 10-day persistence events (56 composited days) at lags -10, -5, 0, 5, and 10 in which lag 0 is the start of the transition from node 8 and lag 10 is the end of the persistence period in node 8. **LEFT:** positive (negative) 500 hPa geopotential height (m) anomalies in red (blue) contoured every 25m starting at 25 (-25) and 250

hPa zonal wind anomalies (ms^{-1}) in red/yellow (blue/purple) contoured every 4 ms^{-1} starting at 4 ms^{-1} (-4 ms^{-1}). Thin gray contours denote structures outside of the 95% significance level. Thick gray contour is the 40 ms^{-1}NDJFM mean isotach. **RIGHT:** positive (negative) SLP anomalies (hPa) in solid (dashed) black lines contoured every 3 hPa starting at 3 hPa (-3 hPa) and 850 hPa temperature anomalies (°K) in red/yellow (blue/purple) contoured every 2 K starting at 2 K (-2 K). Gray solid/dashed contours denote structures outside of the 95% significance level.

Node 8 to 4 10-Day Transition

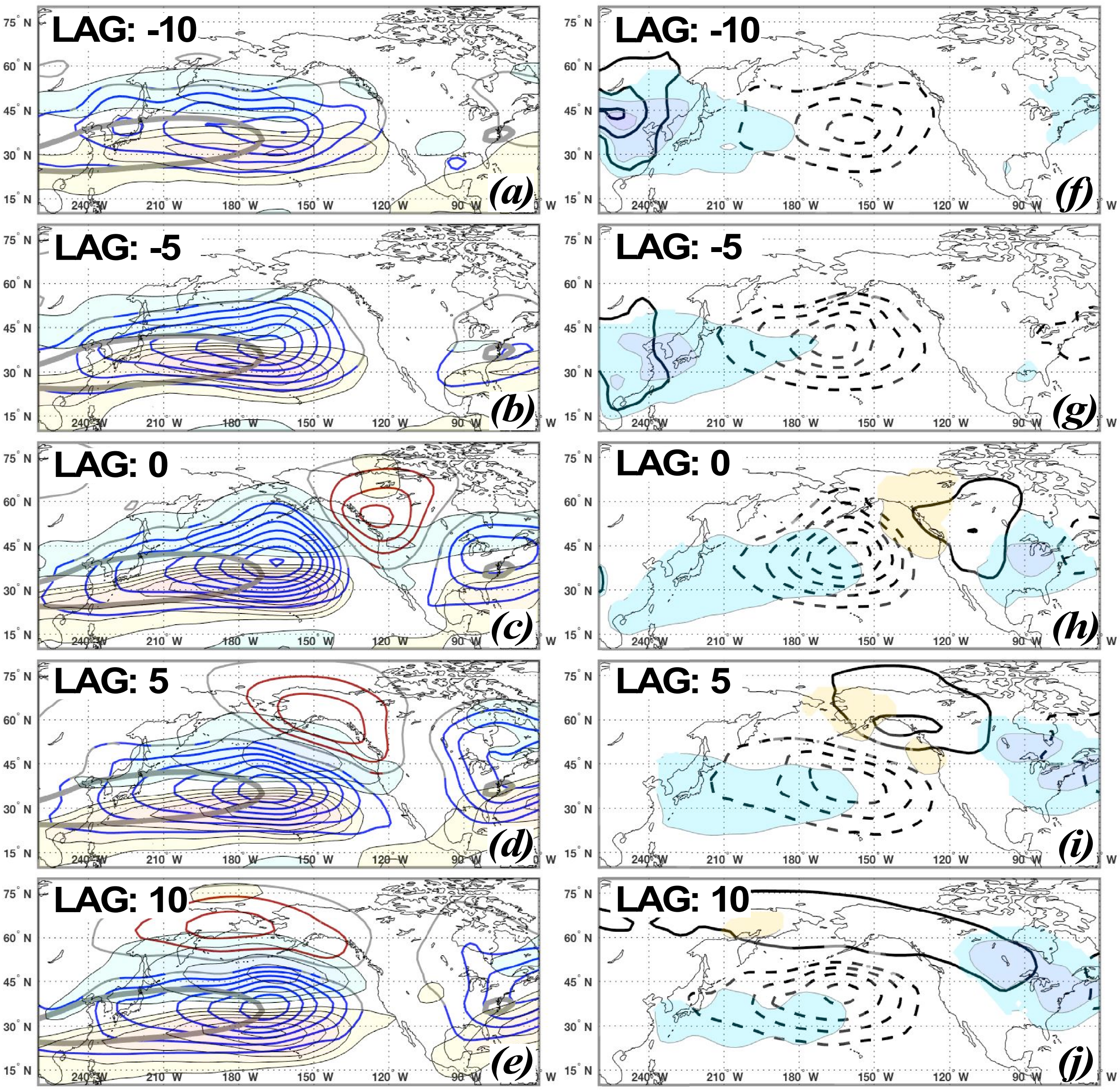

Figure 8. Same as Fig. 7 but for all days within node 8 (defined at lag 0) that transition into node 4 (defined at lag 10) (37 composited days).

Node 5 10-Day Persistence

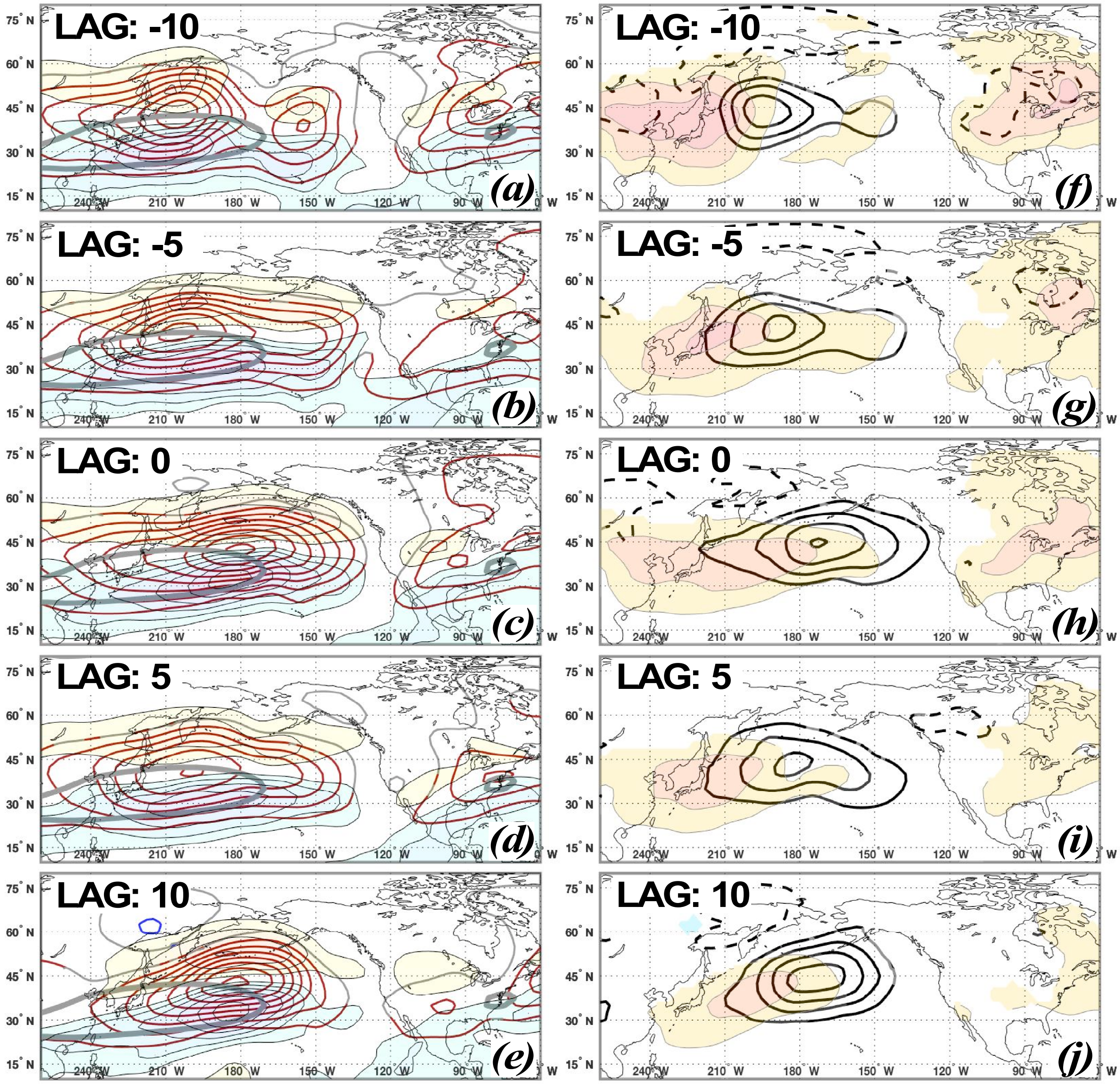

Figure 9. Same as Fig. 7 but for all days within node 5 (defined at lag 0) that persist over 10-days (35 composited days).

Node 5 to 9 10-Day Transition

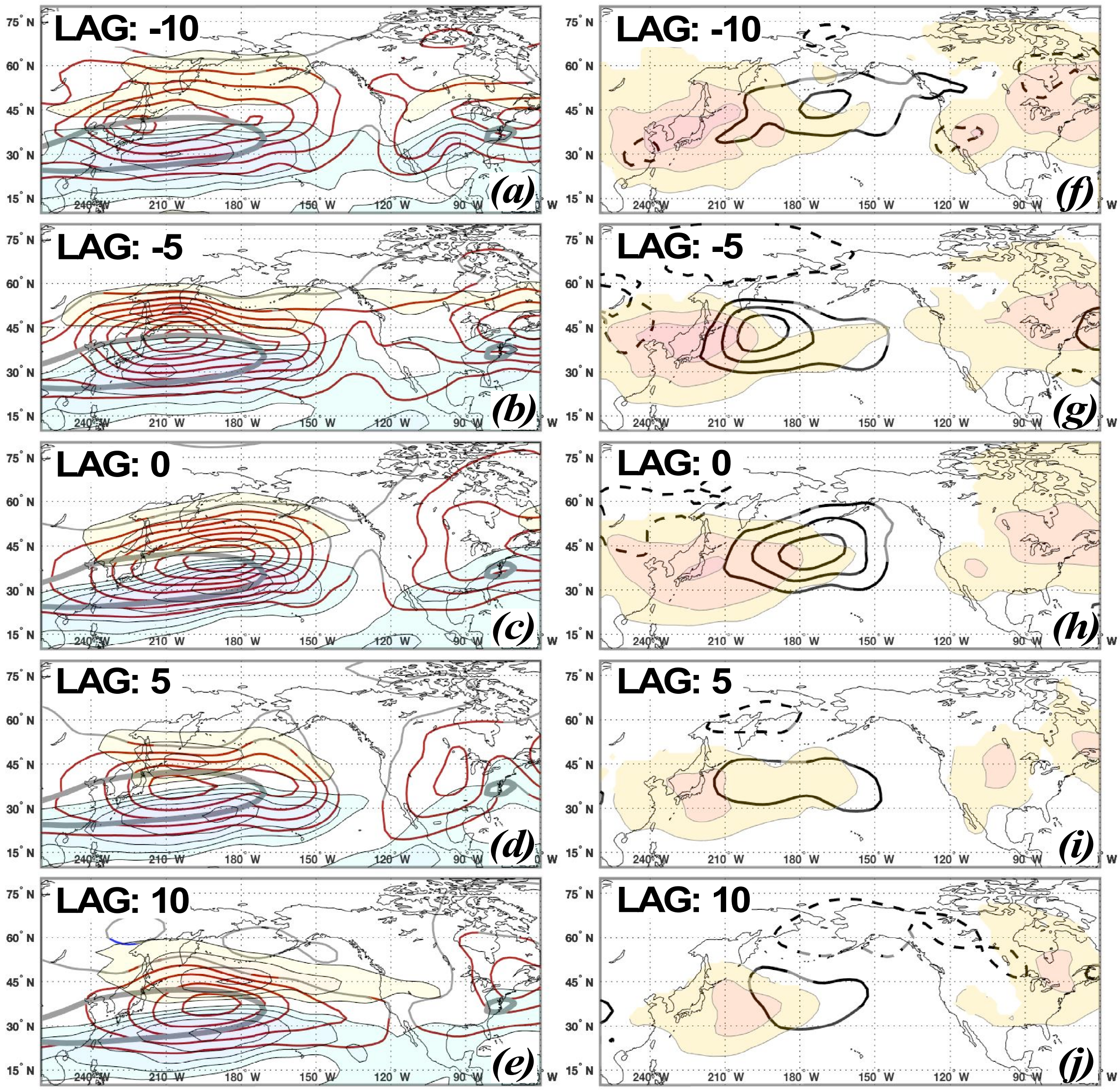

Figure 10. Same as Fig. 7 but for all days within node 5 (defined at lag 0) that transition into node 9 (defined at lag 10) (33 composited days).

Node 5 to 10 10-Day Transition

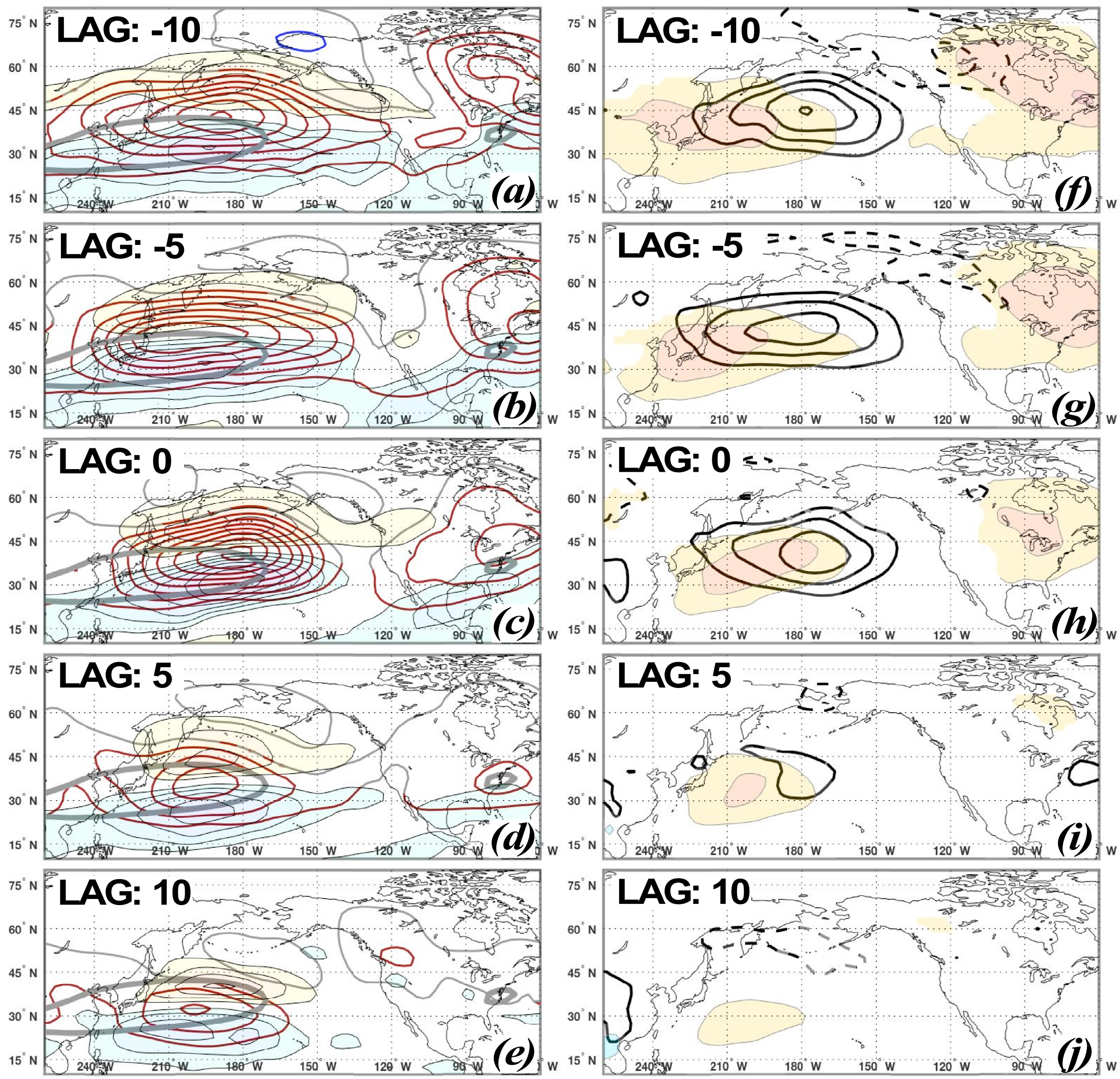

Figure 11. Same as Fig. 7 but for all days within node 5 (defined at lag 0) that transition into node 10 (defined at lag 10) (37 composited days).

Node 2 10-Day Persistence

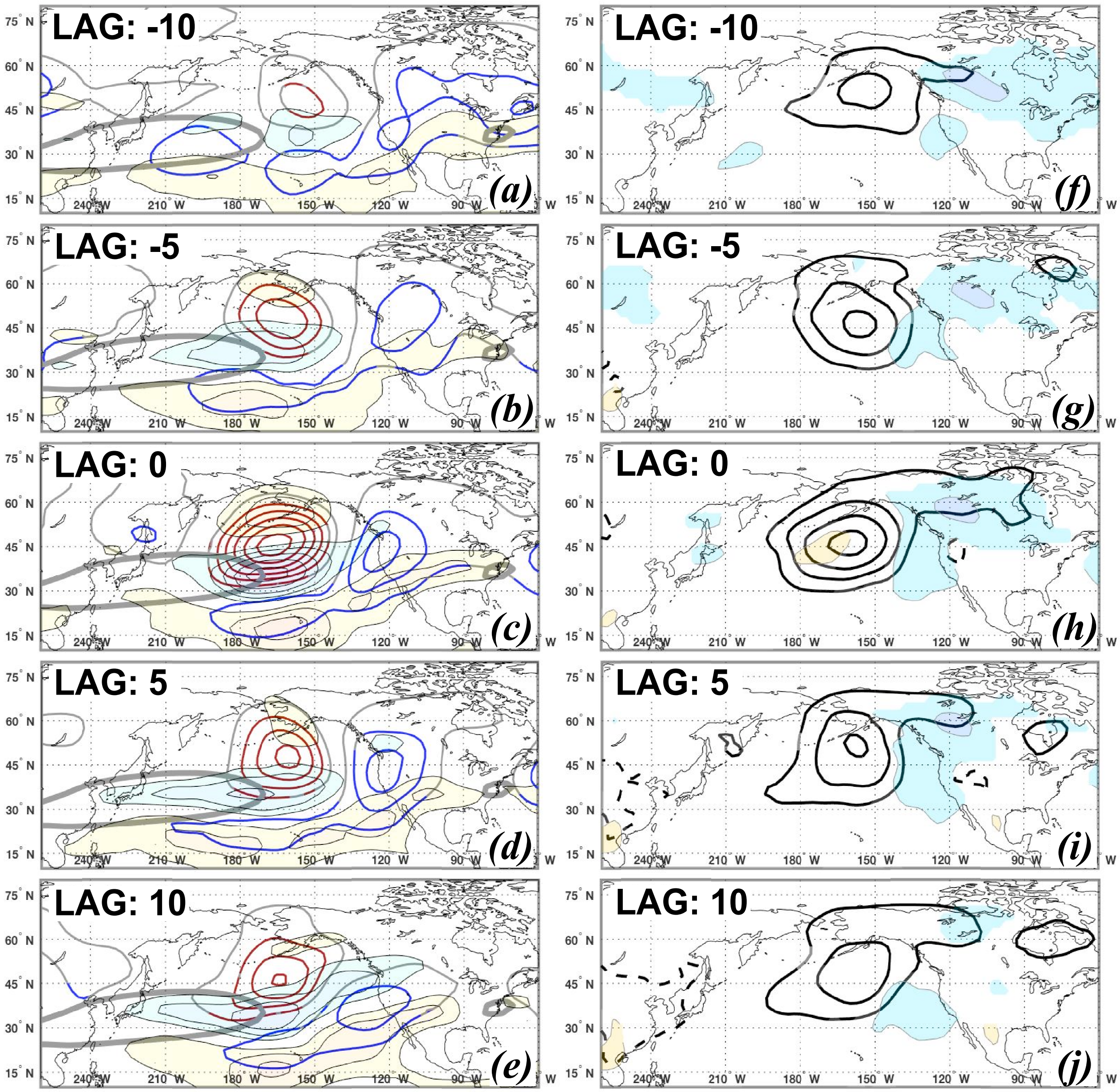

Figure 12. Same as Fig. 7 but for all days within node 2 (defined at lag 0) that persist over 10-days (38 composited days).

Node 2 to 1 10-Day Transition

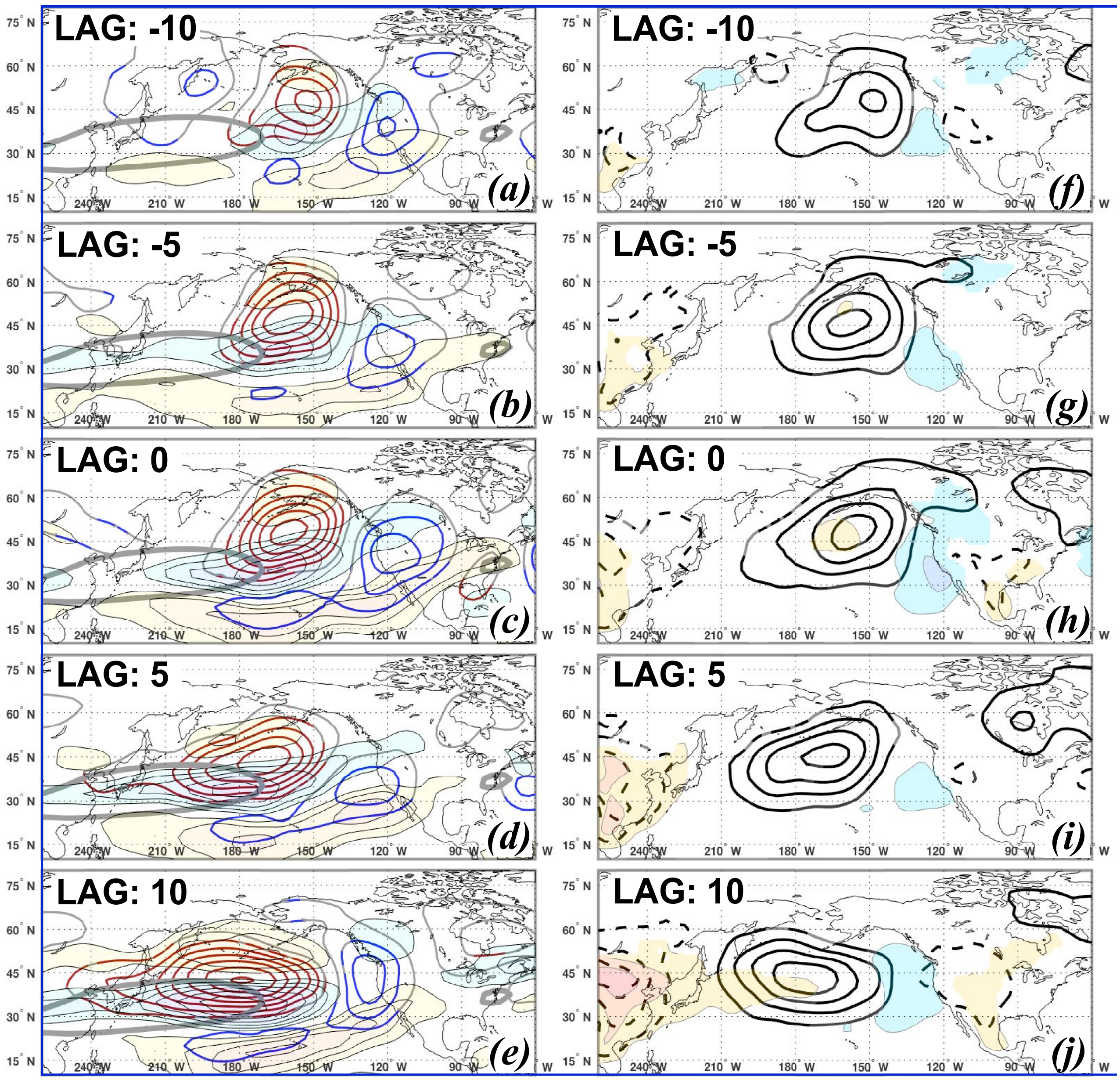

Figure 13. Same as Fig. 7 but for all days within node 2 (defined at lag 0) that transition into node 1 (defined at lag 10) (29 composited days).

Node 2 to 3 10-Day Transition

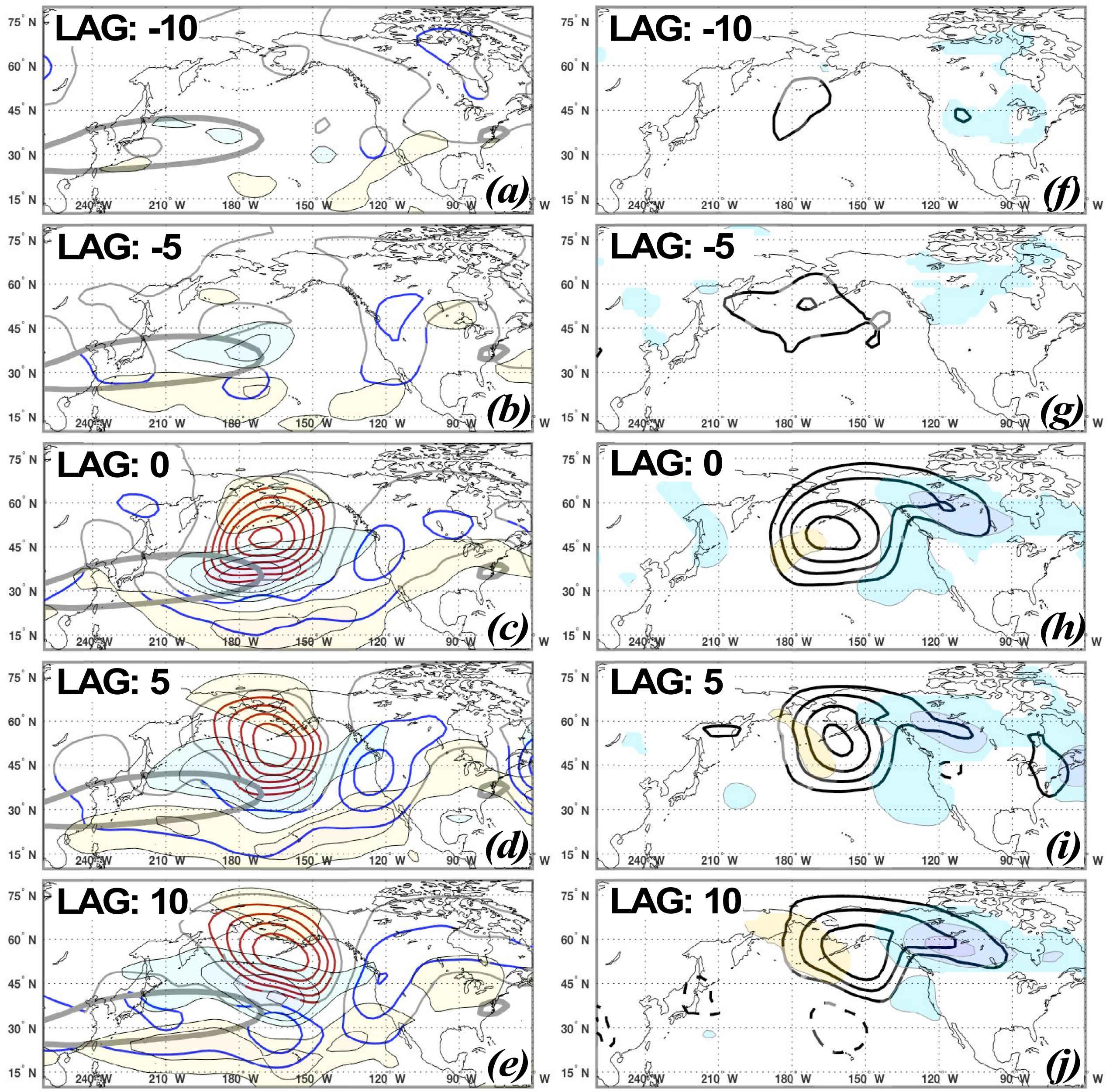

Figure 14. Same as Fig. 7 but for all days within node 2 (defined at lag 0) that transition into node 3 (defined at lag 10) (32 composited days).